

1-1-1974

Models of Saturn's rings which satisfy the optical and infrared observations.

Yoshiyuki, Kawata

University of Massachusetts Amherst

Follow this and additional works at: https://scholarworks.umass.edu/dissertations_1

Recommended Citation

Kawata, Yoshiyuki, "Models of Saturn's rings which satisfy the optical and infrared observations." (1974). *Doctoral Dissertations 1896 - February 2014*. 1867.

https://scholarworks.umass.edu/dissertations_1/1867

This Open Access Dissertation is brought to you for free and open access by ScholarWorks@UMass Amherst. It has been accepted for inclusion in Doctoral Dissertations 1896 - February 2014 by an authorized administrator of ScholarWorks@UMass Amherst. For more information, please contact scholarworks@library.umass.edu.

UMASS/AMHERST



312066 0015 3535 1

MODELS OF SATURN'S RINGS WHICH SATISFY THE
OPTICAL AND INFRARED OBSERVATIONS

A Dissertation Presented

By

Yoshiyuki Kawata

Submitted to the Graduate School of the
University of Massachusetts in partial
fulfillment of the requirements for the degree of

DOCTOR OF PHILOSOPHY

September

1974

Major Subject

Astronomy

Yoshiyuki Kawata 1974

All Rights Reserved

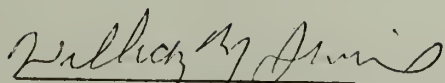
MODELS OF SATURN'S RINGS WHICH SATISFY THE
OPTICAL AND INFRARED OBSERVATIONS

A Dissertation Presented


By

Yoshiyuki Kawata

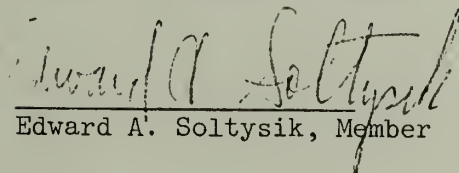
Approved as to style and content by:



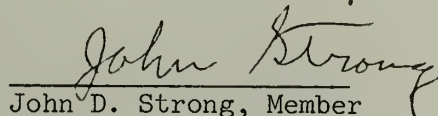
William M. Irvine, Chairman of Committee



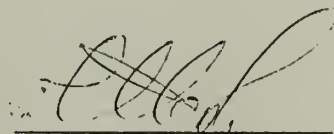
David Van Blerkom, Member



Edward A. Soltysik, Member



John D. Strong, Member



LeRoy F. Cook, Department Head

Department of Physics & Astronomy

September 1974

ACKNOWLEDGEMENTS

I wish to express my deepest gratitude to my advisor, Professor William M. Irvine, for his guidance throughout my thesis project. I would like to express my appreciation to Dr. David Van Blerkom, and Dr. Jeff Cuzzi for their helpful discussions. I also would like to express my gratitude to Professor Sueo Ueno in Japan for his moral support in the completion of this work. I am very grateful to Ms. Terri Grzybowski for her excellent typing of the final manuscript.

I thank my wife, Keiko, for her assistance in the preparation of the thesis draft.

ABSTRACT

The fundamental observations which must be matched by any theoretical model of Saturn's rings is the phase curve of the rings. This phase curve has a very sharp surge in brightness near opposition which is known as the opposition effect.

We assume that a plane-parallel and homogeneous ring layer consists of many independent and randomly oriented spherical particles and that these particles are large enough and their number density great enough to cast shadows upon each other. We assume that the opposition effect is produced by the mutual shadowing of the ring particles (the shadowing mechanism), an idea originally proposed by Seeliger (1887). Under these assumptions we investigate models of Saturn's rings which include this shadowing mechanism, realistic phase functions for the individual ring particles, and the effects of multiple scattering and a particle size dispersion.

In the shadowing mechanism we include the effects due to the finite size of the sun, including the penumbra. The relation $dn = K\rho^{-s} d\rho$ is used for the size dispersion law of the ring particles, where dn is the number of particles with radii between ρ and $\rho + d\rho$, ρ is the radius of a particle, s is a parameter describing the shape of the size distribution, and K is a constant. The parameters of this basic model are limited by the requirement that the absolute brightness of the rings, the variation of brightness with tilt angle (declination of the sun with respect to the ring plane), and the spectra of the rings agree with observation.

The resulting models are considered in relation to the infrared and radar data which are now becoming available. In the calculation of the infrared temperature of the rings, the effect of mutual heating among the ring particles is considered quantitatively for the first time. We find that the effect of mutual heating among the ring particles is stronger than that of the flux from Saturn's ball.

The basic conclusions are the following. Although the monodisperse model and the uniform size distribution model ($s = 0$) work well with the optical data, it seems difficult for them to satisfy the observed high infrared temperature of the rings because of their high optical albedo. The polydisperse $s = 2$ model seems to satisfy both optical and IR data, but the situation could be much clarified if a good phase curve for the rings were available in the red. The possible reasons for the observed color dependence in the opposition effect are discussed. The volume density for ring B is $D \sim 0.01$. The ring particle phase function seems to be moderately backward scattering. The lower limits of the phase integral are found to be $q_B \sim 1.0$ and $g_V \sim 1.4$ in the blue and visual, respectively. The lower limits of the particle albedo are found to be $a_B \sim 0.42$ and $a_V \sim 0.72$. The particle Bond albedos cannot be much higher than those values. The upper limit of a mean particle size is found to be $\langle \rho^2 \rangle^{1/2} \lesssim 4.5$ m. The lower limit on particle size and the mean particle size itself remain uncertain. The lower limit of the optical thickness of ring B is $\tau_{\min} > 0.5$.

The upper limit of the mean particle size found in this model agrees with both the models suggested by Pollack et al. (1973) and Pettengill and Hagfors (1974) to fit the microwave and radar data. The high albedo for ring particles agree with the deduction from the spectral data (Lebofsky et al., 1970) that the principal constituent of at least the outer portions of the ring particles is ice, slightly reddened by either the action of high energy radiation or the presence of impurities.

TABLE OF CONTENTS

	Page
I. Introduction	1
II. Available Photometric Observations and Outline of the Procedure	7
III. Theoretical Procedure for Analyzing the Photometric Observations	11
A. Shadowing Mechanism	12
B. Multiple Scattering	23
IV. Comparison with the Observations	29
V. Allowable Range of Parameters	44
A. Distribution of Particle Size	56
B. Tilt Effect	63
VI. Infrared Brightness Temperature	67
A. Procedure	67
B. Albedo Spectrum	71
C. Result	81
VII. Conclusion	88
References	91

LIST OF TABLES

	Page
Table I. Allowable range of parameters for ring optical thickness $\tau = 1$	39
Table II. Summarized results for ring optical thickness $\tau \neq 1$	54
Table III. Comparison between monodisperse particle size case and polydisperse particle size case.	65

FIGURE CAPTIONS

	Page
Figure 1. Observed phase curves for ring B	8
Figure 2. Geometry of the shadowing effect	13
Figure 3. Magnitude of the shadowing effect $\delta M(D)$ for primary scattering as a function of volume density D	20
Figure 4. Theoretical phase curves for primary scattering with $\tau = 1$	22
Figure 5. Spectral reflectivity of Saturn's rings	34
Figure 6. Diagram for comparison of observation and theory	36
Figure 7. Theoretical phase curves for $\tau = 1$	40
Figure 8. Four sample phase functions Φ used for the calculations illustrated in Figure 6	43
Figure 9. Diagram for comparison of observation and theory for $\tau = 1$ and $R_V^O = 1.0$	46
Figure 10. Theoretical phase curves for $\tau = 0.7$	48
Figure 11. Diagram for comparison of observation and theory for $\tau = 0.7$ and $R_V^O = 1.0$	49
Figure 12. Theoretical phase curves for $\tau = 0.5$	51
Figure 13. Theoretical phase curves for $\tau = 2.0$	52
Figure 14. Diagram for comparison of observation and theory for $\tau = 2.0$ and $R_V^O = 1.0$	53
Figure 15. Diagram for comparison of observation and theory for $\tau = 1.0$ and $R_V^O = 1.1$	55
Figure 16. Theoretical phase curves for $\tau = 1.0$ in the polydisperse cases of $s = 2$ and $s = 3$	60

	Page
Figure 17. Comparison of the ring particle phase curves and those for the Moon and for a Lambert sphere	62
Figure 18. Comparison of the theoretical tilt effect and the observational data	66
Figure 19. Magnitude of the opposition effect for Saturn's rings	73
Figure 20. Ring particle albedo versus wavelength	74
Figure 21. Diagram for comparison of observation and theory in the polydisperse case $s = 2$	76
Figure 22. Four sample phase functions Φ used for the calculations illustrated in Figure 21	77
Figure 23. Diagram which shows the change in the magnitude of the opposition effect as the slope of the linearly increasing portion of the phase curve changes	80
Figure 24. Theoretical IR brightness temperature distribution based on the case A	85
Figure 25. Theoretical IR brightness temperature distribution based on the case B	86
Figure 26. IR brightness temperature for ring B versus $\mu_0 = \cos\theta$	87

LIST OF SYMBOLS

		Page
Symbol	Definition (First Use)	
a	single scattering albedo of the ring particles (Bond albedo)	12
a_V, a_R, a_B, a_{IR}	Bond albedos in the visual (V), red (R) blue (B), and infrared (IR), respectively	3, 33, 43, 69
b, g_1, g_2	parameters of combined Henyey-Greenstein phase functions	28
$B_\lambda(T)$	Planck function	68
dn	number of the ring particles with radii between ρ and $\rho + d\rho$	57
$D = \frac{4}{3} \pi \cdot n \cdot \rho^3$	volume density (fraction of the ring volume occupied by particles)	12
$E^\ominus(\zeta, \mu_0) \cdot K_\lambda$	amount of energy absorbed by the rings from the sun per unit area, unit time, and unit optical depth at optical depth ζ and when the cosine of the solar illumination angle is μ_0	69
E_λ	solar energy flux	70
$f(\rho)$	ring particle size distribution function	57
g	asymmetry factor of Henyey-Greenstein phase function (degree of forward and backward scattering)	27
h	depth of a scattering particle in the ring layer	13
I	specific intensity	11
$I_\ominus(\Omega, \zeta)$	mean intensity of unscattered radiation of optical depth ζ in the direction Ω in the ring layer	25

	Page
I_1^S	primary scattered intensity including shadowing correction 11
I_n	n-th order scattering intensity for the conservative case ($a = 1$) 12
J_λ	mean intensity 67
K_λ	total extension coefficient 68
$M_1(\alpha)$	theoretical phase curve as a function of α for primary scattered reflection 21
$M(\alpha)$	theoretical phase curve as a function of α 29
n	number density of particles in the ring layer 12
p_B, p_V	geometric albedos in B and V, respectively 42
q_B, q_V	phase integrals in B and V, respectively 42
R	total reflected intensity by the rings 24
R_1^S	intensity of primary scattered radiation reflected by the rings including shadowing correction 16
$\langle R_1^S(\theta, \phi) \rangle$	reflected intensity in the direction (θ, ϕ) averaged over the finite size of the sun 18
R_n	intensity of reflected radiation due to n-th order scattering 29
R^O	observed absolute ring brightness at opposition 31
R_B^O, R_V^O, R_R^O	observed absolute ring brightness in B, V, and R, respectively 32, 35
S_λ	source function including thermal contribution 67

	Page
$\langle S(\alpha) \rangle$	averaged intensity of primary scattered radiation reflected by the rings (including shadowing correction) for the case of conservative, isotropic scattering 29
s	parameter describing the shape of the ring particle size distribution 57
t	physical thickness of the ring layer 12
T^*	IR brightness temperature of the rings 82
T^\ominus	IR brightness temperature of the rings due to absorbed solar flux 81
$T^{\ominus+D}$	IR brightness temperature of the rings due to absorbed solar flux plus the mutual heating among the ring particles 81
$T^{\ominus+D+h}$	IR brightness temperature of the rings due to absorbed solar flux, mutual heating, and the flux from Saturn's ball 81
x	parameter describing multiple scattering contribution to the intensity reflected by the rings 30
x_B, x_V	same parameters defined above in B and V, respectively 38
α	phase angle (the angle between the direction of the sun and that of the Earth as seen from the rings) 8
$\delta M(D)$	magnitude difference between the primary scattered reflections at $\alpha = 0^\circ$ and at $\alpha = 6^\circ$ as a function of volume density D 19
$\delta(x)$	Dirac delta function 25
$\zeta = n\pi\rho^2h$	optical depth within the ring layer 14
θ	polar angle with respect to the outward normal to the ring layer 12

	Page
θ_0	polar angle of incidence (solar illumination angle) 12
κ_λ	absorption coefficient 69
λ	wavelength 5
μ	$\equiv \cos\theta $ 12
μ_0	$\equiv \cos\theta_0 $ 12
ϕ	azimuthal angle measured from the plane of incidence 12
ϕ_0	azimuthal angle of solar incident radiation 12
$\pi F'$	incident solar flux normal to the upper surface of the rings 14
$\pi F' (= \pi F' / \mu_0)$	incident solar flux normal to the direction of the sun 31
ρ	particle radius 6
$\tau = n\pi\rho^2 t$	optical thickness of the ring layer 15
$\Phi(\Omega, \Omega_0)$	ring particle phase function for scattering from direction Ω_0 into direction Ω 15
$\Phi_{HG}(\gamma, g)$	Henyey-Greenstein phase function γ is scattering angle and g is asymmetry factor 27
$\Omega = (\theta, \phi)$	direction having polar angle θ and azimuthal angle ϕ 12
$\Omega_0 = (\theta_0, \phi_0)$	direction of the incident solar radiation on the rings 12

S E C T I O N I

INTRODUCTION

The data provided by optical observations have traditionally been the core material for attempts to understand the nature of Saturn's rings. By optical in the present context we mean the extended visible portion of the spectrum (roughly 0.3 - 1.0 microns) in which radiation received at the Earth from Saturn's rings is reflected sunlight, and hence does not include thermal emission by the ring particles. Although critical observations are now becoming available in the infrared and microwave regions of the spectrum, models of Saturn's rings must continue to satisfy the constraints provided by the optical data.

Let us describe the basic information on Saturn's rings. Saturn's ring system was first discovered by Huygens in 1655. Its mean distance from the earth is ~ 9.5 AU. It is known that it consists of three concentric portions, the outer ring A, the middle brightest ring B, and the inner faintest ring C. The radial distance is $\sim 1.4 \times 10^5$ km from the center of Saturn to the outer edge of ring A. The corresponding distance is $\sim 7 \times 10^4$ km from the center of Saturn to the inner edge of ring C. Ring B is separated from ring A by a distinctive gap, the Cassini division. The maximum and minimum radial distances of ring B from the center of Saturn are $\sim 1.2 \times 10^5$ km and $\sim 9 \times 10^4$ km, respectively. The rings lie in the equatorial plane of Saturn and the physical thickness of the rings is estimated to be a few km. The doppler shift in the ring spectrum indicates that the revolution period of the inner portion of the rings about Saturn is shorter than that of

the outer portion of the rings. This indicates that the rings have differential rotation and the ring system is not a solid sheet, but instead a swarm of orbiting particles. The above data are taken from Bobrov's Saturn's rings survey (Bobrov, 1970).

Maxwell (1859) studied the stability condition for a ring of non-colliding particles. His stability criterion is that the rings will be stable if the density of the ring is less than one-three hundredth of the density of Saturn. Since Maxwell neglected the ring's differential rotation, his upper limit of the ring density was greatly underestimated. Cook and Franklin (1964, 1966) rediscussed Maxwell's study and found that the upper limit of the ring density must be raised by more than a factor of 10. The effect of collisions among the ring particles was discussed by Jeffreys (1947). In the discussion, he concluded that the rings should transform into a collisionless system one particle thick because of the energy dissipation due to the partly inelastic collisions. Since a ring system one particle thick makes it difficult to explain the observed brightness surge near opposition, it is necessary to find mechanisms of energy replenishment which are able to prevent the full flattening of the rings during the lifetime of the solar system. Since the differential rotation causes the transfer of angular momentum along the rings, the above energy source may be the differential rotation of the rings.

The nature of the ring particles is still a matter of considerable controversy. Let us review briefly the historical background on the investigation of Saturn's rings bearing on this question. The observations of Müller (1893) indicated for the first time an unusual

increase in brightness of the rings near opposition.

Seeliger (1887, 1893) explained this effect (known as the opposition effect) by the mutual shadows cast among big particles in the rings. The basis of this theory is discussed more fully in section II below. Since Seeliger's theory did not agree well with more accurate measurements of the surface brightness of the rings as a function of the phase angle (the angle between the direction of the sun and that of the earth as seen from the rings) obtained by Guthnick and Prager (1918), Hertzsprung (1919) and Schoenberg (1922), an alternative explanation was considered.

Schoenberg (1933) proposed that the opposition effect was due to diffraction by very small ring particles. Since the best observations at that time suggested ripples in the phase curve, and since the number of ripples depends on the particle radius according to diffraction theory, Schoenberg found a mean particle radius of 1.8μ by comparing the theory with observations. We may, thus, understand that the size of a ring particle will be big relative to the wavelength according to Seeliger's theory, while it will be of the same order as the wavelength from Schoenberg's point of view.

Seeliger's original theory was improved in a series of papers (1940, 1956, 1961, 1970) by Bobrov. He included three factors which were ignored by Seeliger: the effect of the finite size of the sun, the multiple scattering contribution to the brightness, and the size dispersion of the ring particles. In 1961 Bobrov also showed that the high surface brightness of the ring B could not be explained by diffraction, as Schoenberg had proposed. The particle albedo a_v in

the visible for ring B was estimated to be about $0.5 \sim 0.6$ by Bobrov.

A wavelength dependence of the opposition effect was reported by Franklin and Cook (1965) and more recently by Irvine and Lane (1973). Franklin and Cook (1965) considered the possibility that either the glory in the backward scattering by the individual ring particles or the diffraction by small ring particles into their shadows was responsible for the wavelength dependence of the opposition effect. The later possibility is not allowed, because it leads to a ring thickness of 10 cm, which seems too thin, as compared with observed ring thickness of 2 km (Kiladze 1969; Focas and Dollfus 1969). In a reworking of their previous paper Cook et al. (1973) obtained $a_V \sim 0.6$.

After studying the measurements of the ring's surface brightness as a function of the declination angles of the sun and the earth with respect to the ring plane, Lumme (1970) and Price (1973) concluded that the effect of multiple scattering in the ring system should be quite large, and the particle albedo, therefore, should be ~ 0.9 in the visual.

Concerning the particle albedo, the infrared temperature measurements will provide us important information. Allen and Murdock (1971) obtained an infrared temperature of the ring B which was $\sim 83^\circ\text{K}$. More recent infrared observations by Murphy (1973) and Morrison (1973) suggest even higher ring temperatures in the infrared, about 90°K . These results indicate that the ring brightness temperature in the infrared is much higher than previously thought, and impose a corresponding constraint on the values of the visible albedo.

The attempts to identify the possible ring constituents have been made by comparing infrared spectral data in the laboratory with that of

the rings. The recent infrared spectra of the rings by Kuiper et al. (1970) show strong absorption bands near 1.5, 1.66, 2.0, and 3.0 microns. Pilcher et al. (1970) show that H_2O frost, originally proposed as a ring constituent by Kuiper (1949), is in better agreement with the new ring spectrum than is NH_3 frost (proposed by Kuiper et al., 1970).

In addition to infrared observations, recent radar observations at $\lambda = 12.6$ cm by Goldstein and Morris (1973) for the first time detected radar echos from the rings. The signal was surprisingly high. Goldstein and Morris suggest meter size particles in the ring system from their interpretation of the radar results. According to this interpretation, the observed high radar reflectivity is simply due to strong backward scattering by large (compared to the wavelength), rough ring particles. Since this "meter size" model leads to a much higher brightness temperature in the microwave region than the observed upper bound brightness temperature of the rings, Pollack et al. (1973) propose that the high radar reflectivity is the result of multiple scattering by ring particles having a high single scattering albedo at the wavelength of observation. From this "bright cloud" model the latter authors obtained a mean particle radius ~ 2 cm. Pettengill and Hagfors (1974) proposed a model which does not conflict with either high radar return or low observed brightness temperature in the microwave region. They consider the ring particles to be nearly transparent spheres. Since such particles absorb very little solar energy, they are consequently poor radiators of thermal energy. The high radar return is explained by the fact that backscattering from nearly transparent spheres can show considerable gain over the simple external reflection

from spheres having a large dielectric constant, such as the rough particles proposed by Goldstein and Morris. They showed that any such sphere in the size range $8 < \rho < 200$ cm (ρ is the particle radius) has much larger backscatter cross section than that required for the radar observation.

Previous analyses of the optical observations have suffered from limitations which are no longer necessary in view of improved computational and theoretical methods. We have accordingly endeavored to apply the best procedures currently available in an effort to see what limitations the optical data impose upon the physical parameters of the ring system and the particles which it contains. The procedure which we shall use (Section III) is a refinement of that originally proposed by Seeliger (1887) and subsequently employed in the fundamentally important work of Bobrov (e.g., 1970) and Franklin and Cook (1965). We shall compare the theoretical model with the optical observations (Sections IV and V). The resulting model will then be considered in relation to the new infrared and radar data (Section VI).

S E C T I O N I I

AVAILABLE PHOTOMETRIC OBSERVATIONS AND OUTLINE OF THE PROCEDURE

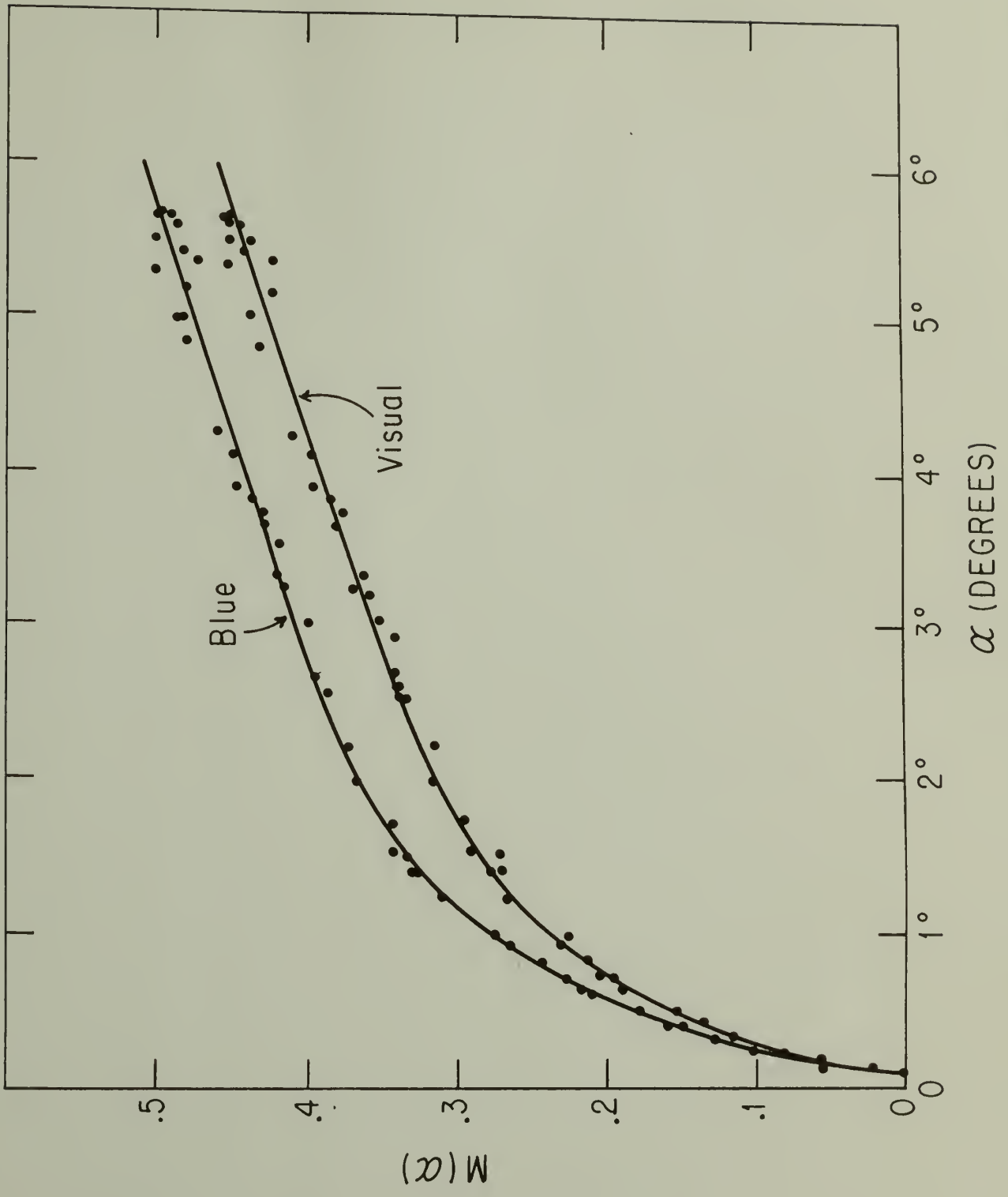
Since the most complete and reliable photometric data are available only for the bright ring B, we shall concentrate our attention on this ring. The fundamental observation which must be matched by any theoretical model is the phase curve of the rings; that is, the surface brightness normalized at phase angle 0 versus phase angle α . This curve is normally plotted in stellar magnitudes per square arc-second of the rings, and has the following three characteristic features:

1. A very sharp surge in brightness near $\alpha = 0^\circ$ which is known as the opposition effect;
2. A linearly decreasing brightness as α increases for $\alpha > 2^\circ$;
3. A dependence upon wavelength.

The most reliable photometric phase curves appear to be those of Franklin and Cook (1965) which were obtained in the B and V wavelength bands (effective wavelengths $\lambda = 0.448\mu$, and $\lambda = 0.564\mu$, respectively). These data are illustrated in Figure 1. Since Saturn did not reach exact opposition ($\alpha = 0^\circ$) during their observations and the extrapolation to $\alpha = 0^\circ$ is somewhat arbitrary, we have normalized all data at the minimum phase angle observed ($\alpha = 0.094^\circ$).

Another observation of critical importance to the understanding of the rings is the absolute surface brightness as a function of wavelength. Data for B and V were obtained by Franklin and Cook (1965). Corresponding data for other wavelengths may be obtained from the relative spectral photometry of Lebofsky et al. (1970), Irvine and Lane (1973),

Figure 1: Phase curves (surface brightness versus phase angle α)
for ring B at two wavelengths normalized at $\alpha = 0.094^\circ$
(from Franklin and Cook, 1965).



and Kharitonova and Teifel (1973), although care must be taken to insure that observations made under corresponding conditions are compared. This is important because the brightness of the rings may depend upon a number of geometric factors, including α and declination of the sun and earth relative to the ring plane, and possibly on the distance of Saturn from the sun or the position of the ring particles relative to their eclipse by Saturn. Complete phase curves of the rings at wavelengths in the red and near ultraviolet would be most desirable in the future.

Additional photometric observations of potential importance are the variation in ring brightness with declination of the sun and earth. Observations have been made by Camichel (1958) and Price (1973).

The principal diagnostic characteristic of the phase curve is the opposition effect. We shall proceed on the assumption that this effect is produced by the mutual shadowing of the ring particles, an idea originally proposed by Seeliger (1887). In more detail, we assume that the rings consist of a plane layer containing many independent particles which are illuminated by the sun and observed from the earth. Those particles nearer the sun cast shadows upon the particles behind. At exact opposition an observer on earth will see only sunlit particles and so will observe a maximum surface brightness. As the phase angle increases, the shadowed particles which were formerly shielded from view by the sunlit particles may now be observed from the earth, so that the surface brightness falls off. This initial decrease in brightness takes place very rapidly as a function of phase angle.

Observations of stellar occultations by Saturn's rings indicate that the optical thickness of ring B is near unity. Because of the relatively high albedo of the ring particles (cf. Lumme, 1970; Price, 1973; Cook et al., 1973), it then follows that multiple scattering will play an important role in determining the photometric properties of the ring system. In previous computations of the shadowing mechanism multiple scattering has been included in only an approximate manner, by assuming that higher order scattering will be isotropic. We treat rigorously the multiple scattering problem for more realistic, anisotropic particle phase functions, including wavelength dependence.

The close relationship between the shadowing mechanism described above and the usual multiple scattering theory of radiative transfer has been discussed by Irvine (1966). Radiative transfer theory can be applied when the interparticle distance in the layer is sufficiently large that each particle is effectively in the far field for scattering by the other particles, so that shadows may be neglected. When the particles are large enough and their number density is great enough, they will cast shadows upon each other, and the usual multiple scattering theory must be modified to include the effect of shadowing. Fortunately, this can be done in a straight-forward manner.

S E C T I O N I I I
 T H E O R E T I C A L P R O C E D U R E F O R A N A L Y Z I N G
 T H E P H O T O M E T R I C O B S E R V A T I O N S

We shall assume in our model that the rings are plane-parallel and homogeneous with respect to optical depth. We thus neglect the possibility that such properties as mean particle size or composition depend on altitude with respect to the center of the ring plane. We shall furthermore assume for the present that the ring particles may be characterized by a single effective radius ρ and for the purposes of the shadowing computation may be treated as spheres. We shall return in Section V below to the possibility of a distribution of particle sizes, which introduces into the theory such quantities as $\langle \rho^2 \rangle^{1/2}$ and $\langle \rho^3 \rangle^{1/3}$ in addition to the mean radius $\langle \rho \rangle$. The assumption of sphericity will not significantly effect the applicability of our results, since it can be shown that the magnitude of the shadowing effect at opposition is independent of the particle shape (Seeliger, 1895), and we do not require that the individual particle phase function be given by Mie theory.

Following the procedure of Irvine (1966), we may express the specific intensity I of the radiation reflected by the rings as a sum of successive orders of scattering:

$$I = I_1^S + \sum_{n=2}^{\infty} I_n a^n \quad (1)$$

where I_1^S is the contribution from once-scattered radiation including the necessary shadowing correction, and $a^n I_n$ is the contribution from

radiation scattered n times (a is the single scattering albedo of the ring particles, and I_n is the n -th order scattering intensity for $a = 1.0$. See equation (3) below). Fortunately, the effect of mutual shadowing is important only in the calculation of the primary scattered intensity and may be neglected in the computation of I_n for $n \geq 2$.

A. Shadowing Mechanism. Let us discuss first the computation of I_1^s . If the wavelength of light λ is such that

$$\lambda \ll \rho^2/\Delta$$

where Δ is the lesser of the mean free path of a photon in the layer and the thickness of the layer, a shadow will be formed behind each particle which will be described by geometric optics (van de Hulst, 1957). Let us introduce coordinates such that $\theta = \arccos \mu$ is the polar angle with respect to the outward normal to the ring layer and ϕ is the corresponding azimuthal angle measured from the plane of incidence. We shall use the notation $\Omega = (\theta, \phi)$ to specify a particular direction, and shall initially assume that solar radiation is incident only in the direction $\Omega_0 = (\theta_0, \phi_0)$. For convenience we take $\mu_0 \equiv |\cos \theta_0|$. Let the physical thickness of the ring layer be t , and let the fraction of the ring volume occupied by particles be D , so that

$$D = \frac{4}{3}\pi \rho^3 n \quad (2)$$

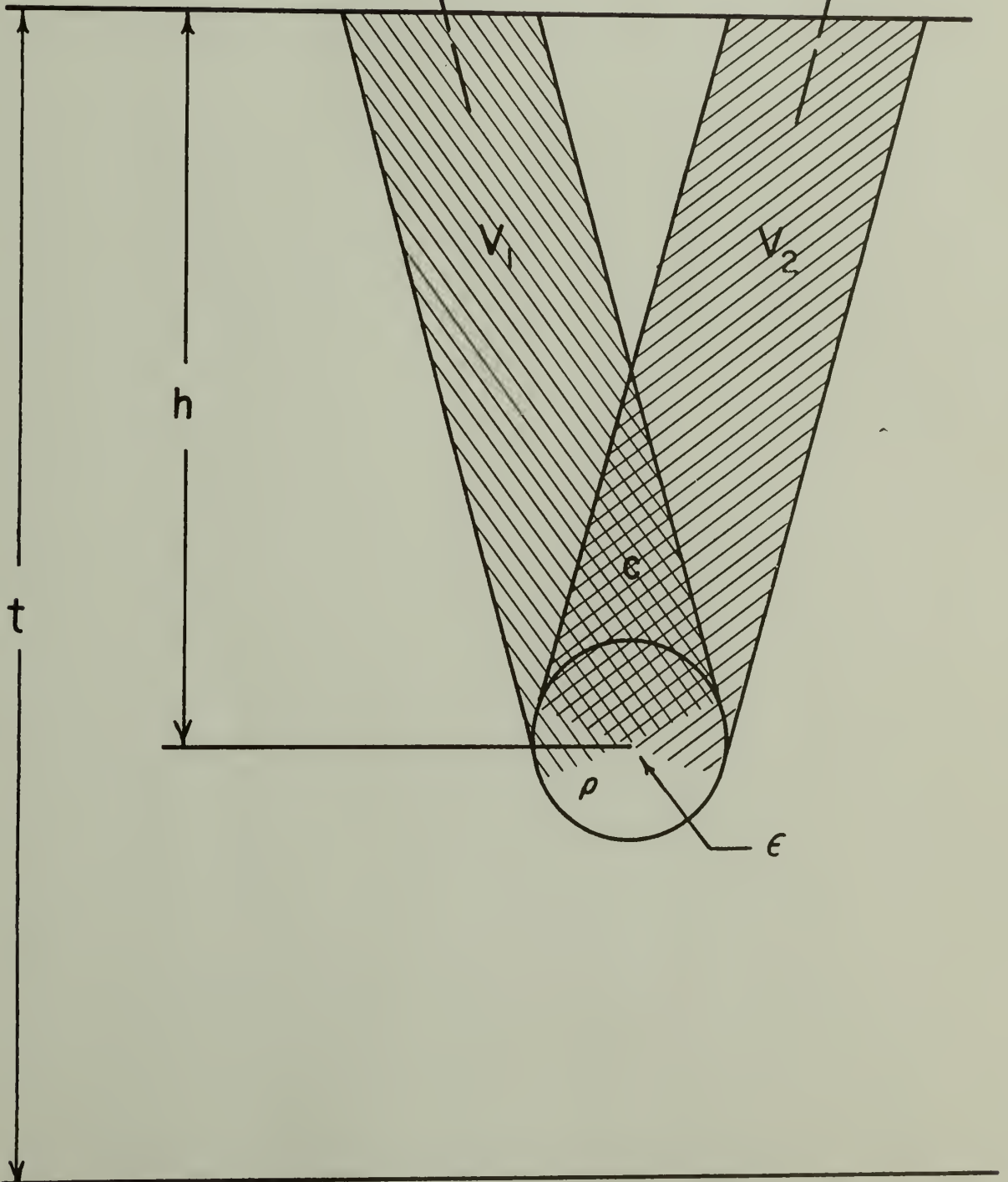
where n is the number density of particles in the rings.

The physical mechanism operative in the shadowing effect can be understood by referring to Figure 2, which shows a particle of radius ρ

Figure 2: Geometry of the shadowing effect. Direction toward the sun in $\Omega_o = (\theta_o, \phi_o)$, towards the earth is $\Omega = (\theta, \phi)$. Thickness of the ring layer is t , depth of particle of radius ρ from the ring surface is h .

$$\Omega_0 = (\theta_0, \phi_0)$$

$$\Omega = (\theta, \phi)$$



at a depth h within the ring layer. The volumes V_1 and V_2 are (except for a small correction near the surface) cylinders of base area $\pi\rho^2$ and height h/μ_0 and h/μ , respectively. A small element ε of the projected area of the particle will be both sunlit and observable from the earth provided that the centers of all other particles in the ring layer are outside of the volumes V_1 and V_2 . If, as implied by our postulate of homogeneity, the ring particles are randomly distributed through the ring volume, the probability of the above situation occurring may be easily computed given the assumption that the fractional volume occupied by particles is sufficiently small ($8D \ll 1$). This probabilistic approach yields the familiar exponential attenuation for both the average radiation field at a depth h in the layer and for the primary scattered radiation emerging from the layer, provided that the volumes V_1 and V_2 do not significantly overlap. If they do so overlap, an anomalously high intensity is produced because the probability for photon escape from a depth h becomes highly correlated with the probability of photon penetration to the same point. This is the shadowing effect.

The analysis shows that, if the incident solar flux through the upper surface is $\pi F'$, the single-scattered intensity at an optical depth $\zeta = n\rho^2 h$ traveling in a direction Ω is given by

$$I_1^s = \frac{a \phi(\Omega, \Omega_0) F' e^{\zeta/\mu}}{4\mu \mu_0} \int_{\zeta}^{\tau} d\zeta' \exp[-\zeta'(\mu^{-1} + \mu_0^{-1}) + nC] \quad (3)$$

where n is the number density of particles, C is the overlap volume shown in Figure 2, a is the single-scattering albedo of the ring particles, τ is the optical thickness of the ring layer given by equation (4), the particle phase function is Φ , and the polar angles of incident and scattered light $\arccos \mu_0$ and $\arccos \mu$ are measured from the outward normal. The phase function $\Phi(\gamma)$ defines the probability that a scattered photon will be deviated by an angle γ (see equations (22) and (23)). When $C = 0$, I_1^S is the primary scattering obtained from the usual multiple scattering theory. Since we have assumed that the particles are large and diffraction may be neglected (that is, the efficiency factor for extinction is unity), the optical thickness of the rings is related to the parameters previously introduced by

$$\tau = n\pi\rho^2t \quad (4)$$

The quantity nC has the form (Irvine, 1966)

$$nC = \begin{cases} \nu_1 & (\zeta' - \zeta \leq, \alpha \neq 0) \\ \nu_1 - \Sigma & (\zeta' - \zeta \leq, \alpha \neq 0) \\ (\zeta' - \zeta)/\mu_0 & (\alpha = 0) \end{cases} \quad (5)$$

where

$$v_1 = \frac{(1 + \cos\alpha) D}{\pi \sin\alpha}$$

$$\Sigma = \frac{3(\cos\theta + \cos\theta_0)^2 D}{4\pi \sin\alpha \cos\theta \cos\theta_0 \cos v} \left[\cos\psi - \frac{\cos^3\psi}{3} - (\pi/2 - \psi) \sin\psi \right]$$

$$\cos\alpha = \cos\theta \cos\theta_0 + \sin\theta \sin\theta_0 \cos(\phi - \phi_0)$$

$$\cos\delta = (\cos\theta_0 - \cos\theta \cos\alpha) / (\sin\theta \sin\alpha)$$

$$\tan v = \sin\theta \sin\delta \sin\alpha / (\cos\theta + \cos\theta_0)$$

$$\sin\psi = \frac{4}{3} \frac{(\zeta' - \zeta) \sin\alpha \cos v}{(\cos\theta + \cos\theta_0) D}$$

$$Z = \frac{3}{4} \frac{(\cos\theta + \cos\theta_0)}{\sin\alpha \cos v}$$

When $\zeta = 0$ (i.e., at the surface of the rings), we find the reflected intensity as

$$R_1^S \equiv I_1^S(\zeta = 0) \quad (\mu > 0) . \quad (6)$$

The above approach is essentially that used by Seeliger (1887). Because of the geometry in Figure 2, it is referred to as the cylinder-cylinder model. Bobrov (cf. 1970) has pointed out the important effect introduced by the finite angular diameter of the sun at the distance of Saturn. Because the shape of the shadow volume

will be a cone for light coming from an extended source, he modified the previous theory by replacing the volume V_1 in Figure 2 by a conical volume, producing a "cone-cylinder model". This procedure, however, ignores the penumbra of the shadows cast.

Franklin and Cook (1965) observed that the opposition effect appears to be wavelength dependent, and proposed a model in which this dependence was produced by the wavelength variation of diffraction into the shadow zone. They treated this situation by using a "cone-cone" model for the shadowed volumes, with the dimensions of the "diffraction cone" being wavelength dependent. This model led to an unreasonably small physical thickness of the ring, however, and it is desirable to search for an alternative mechanism for producing the wavelength dependence. Franklin and Cook also considered the possibility that the wavelength effect might be due to differences in the glory produced by small Mie-scattering spheres forming a surface structure on larger particles. For spherical particles there is a contribution to the scattering in the nearly backward direction from edge rays, apparently connected with surface waves generated on the sphere. This enhanced scattering in the backward direction is known as glory (Liou and Hansen, 1971). The glory is observed in nature for water drops. (For example, when we see a bright ring around an airplane shadow projected upon clouds.) This explanation seems extremely unlikely, however, because of the high degree of symmetry of the scattering centers needed to produce the glory phenomenon.

In the present model we propose to take into account the effect of the sun's finite size by performing a numerical average of the intensity obtained under the assumption of a point (infinitely distant) sun. This will rigorously include the effect of the penumbra and also any influence of solar limb darkening. The computation can be carried out quite rigorously, because the necessary arithmetic in equations (3) and (5) is efficiently and rapidly performed on an electronic computer. The resulting model will have a reduced opposition effect relative to the point sun model, because there is no longer an exact opposition for the total solar flux.

If the angular diameter of the sun at Saturn's distance is β (about three minutes of arc), and the sun is assumed symmetric about the angular direction $\Omega_{00} = (\theta_{00}, 0)$ of its midpoint, the average reflected intensity in the direction (θ, ϕ) will be

$$\langle R_1^s(\theta, \phi) \rangle \equiv \frac{\int_0^{\beta/2} d\theta' \int_0^{2\pi} d\phi' \sin\theta' W(\cos\theta') R_1^s[\theta, \phi; \theta_0(\Omega'), \phi_0(\Omega')] \cos\theta_0(\Omega')}{\int_0^{\beta/2} d\theta' \int_0^{2\pi} d\phi' \sin\theta' W(\cos\theta') \cos\theta_0(\Omega')} \quad (7)$$

where the solar limb darkening

$$W(\mu') = a_\lambda + b_\lambda \mu' + c_\lambda [1 - \mu' \ln(1 + (\mu')^{-1})]$$

$$\mu' = \cos\theta'$$

is taken from Pierce and Waddell (1961), who give measured values for

the three empirical constant a_λ , b_λ , and c_λ . The primed coordinates are measured with respect to the direction Ω_{oo} as the polar axis. The relevant angles may be obtained from spherical trigonometry as

$$\cos\theta_o = \cos\theta' \cos\theta_{oo} - \sin\theta' \sin\theta_{oo} \cos\phi'$$

$$\sin\phi_o = \sin\theta' \frac{\sin\phi'}{\sin\theta_o}$$

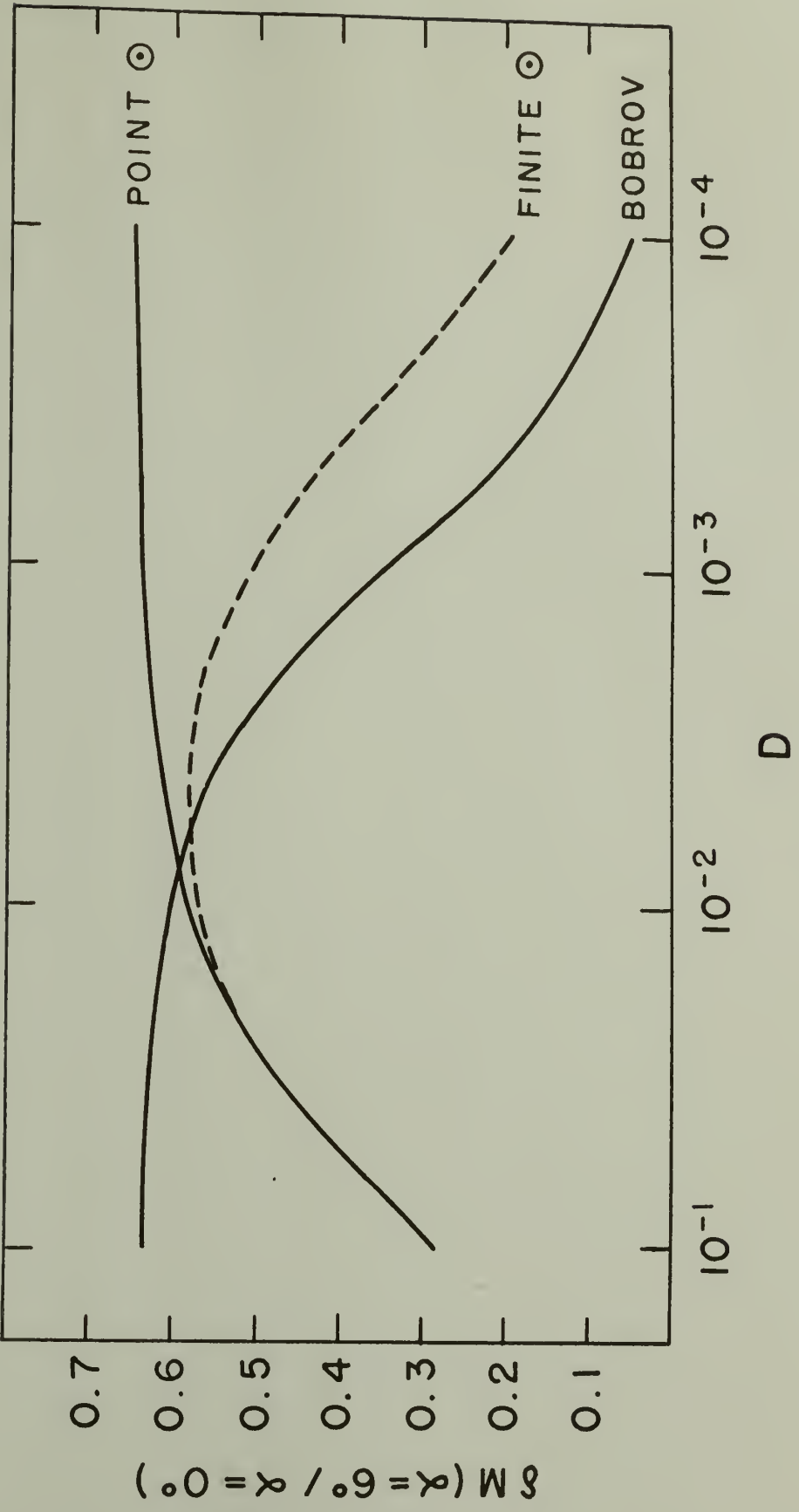
The integrations were carried out by a Gaussian procedure using as many as 14 points in both θ and ϕ . The results are quite insensitive to the particular limb darkening law chosen.

One measure of the theoretical amplitude of the mutual shadowing effect which provides some insight into the differences between the present model and previous ones is the difference $\delta M(D)$ in stellar magnitudes between the primary scattered reflection at $\alpha = 0^\circ$ (where the shadowing effect is maximum) and at $\alpha = 6^\circ$ (where its effect is small):

$$\delta M(D) = - 2.5 \log \frac{[R_1^S(\alpha = 6^\circ)]}{[R_1^S(\alpha = 0^\circ)]} . \quad (8)$$

We have written $\delta M(D)$, because the volume density D is the principal parameter determining the strength of the shadowing effect. Figure 3 presents results of computations for $\delta M(D)$ for the case $\tau = 1$, $\theta = \theta_o = 64^\circ$ (which approximates the Saturnocentric declination of the sun and earth during the observations of Franklin and Cook), and $\phi = 1$. The notation "point Θ " refers to results based on the cylinder-

Figure 3: Magnitude of the shadowing effect $\delta M(D)$ for primary scattering as a function of volume density D (fractional volume occupied by the ring particles) for three different models (see text), ring geometry appropriate to Franklin and Cook (1965) data, and optical thickness $\tau = 1.0$. See equation (8).



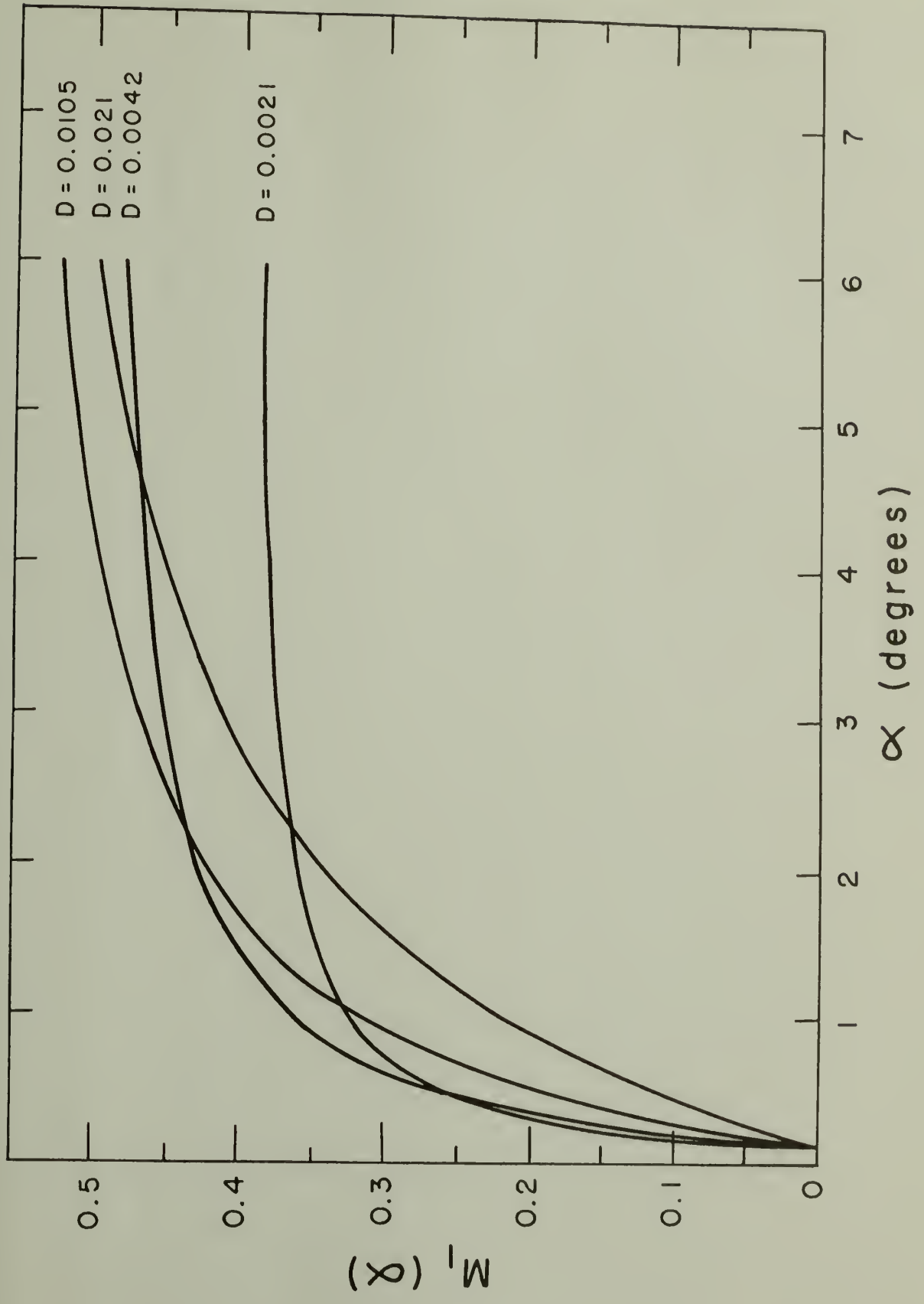
cylinder model described above; "finite Θ " represents the refined cylindrical model which we shall employ and which is described by Equation (7); and "Bobrov" refers to the cone-cylinder model of that author (see Bobrov, 1970).

For both the point Θ and the finite Θ models the shadowing effect (neglecting multiple scattering) decreases for large volume densities because the surface of the rings appears to become smoother (uniformly filled). Because of certain simplifying assumptions in the mathematics, the Bobrov model does not exhibit this behavior. For very small values of D , the point Θ model approaches an asymptotic value for δM ; this behavior is a result of the infinite extent of the cylindrical shadows, and the fact that for a given optical depth τ , as D decreases, the thickness of the layer t must increase (see equation (4)). In contrast, both the finite Θ and Bobrov models produce shadows of finite length, so that for sufficiently small D (sufficiently large inter-particle distance) the shadowing effect vanishes. The Bobrov model produces a smaller shadowing effect for small D because of inaccuracies in its treatment of the penumbra.

A more detailed view of the relation between δM and D may be obtained by considering the entire phase curve $M_1(\alpha)$ as a function of D . Sample phase curves for various D computed from our shadowing theory are shown in Figure 4 for the same parameters used in Figure 3. We note the following points:

1. The smaller the volume density D , the steeper the initial decrease in brightness with increasing phase angle (that is, the more

Figure 4: Theoretical phase curves for primary scattering with $\tau = 1$, $\theta = \theta_0 = 64^\circ$. Curves labeled with the density parameter D .



peaked is the opposition effect).

2. For $D \lesssim 0.01$, the total shadowing effect δM over the phase angle range $0 - 6^\circ$ increases as D increases.

3. For $D \gtrsim 0.01$, the opposition effect has become so broad that δM begins to decrease although the phase curve is still falling off at 6° . We should point out that the values of δM in Figure 4 differ from those in Figure 3 for the same D because in the former case they have been normalized at $\alpha = 0.094^\circ$ for comparison with the data of Franklin and Cook, while in the latter case the normalization was at exact opposition ($\alpha = 0^\circ$).

In fact none of the curves presented in Figure 4 agrees with the data (cf. Figure 1). If the theoretical curves are sufficiently steep for small phase angles, they are too flat for $\alpha \gtrsim 2^\circ$. We therefore must consider the additional effects of the particle phase function Φ and of higher order scattering (next section). Note, however, that since the sharp opposition peak is primarily the result of the shadowing mechanism and not these other effects, we may say from a comparison of Figures 1 and 4 that $D \lesssim 0.02$ if we are to produce a sufficiently sharp peak.

B. Multiple Scattering. It seems to us reasonable to suppose that the wavelength dependence of the phase curve may be due largely to variation of the single-scattering albedo a of the particles. The spectra obtained by Lebofsky et al. (1970) show that the ring reflectivity varies significantly between the ultraviolet and the infrared. Increasing the value of a will significantly change the multiply

scattered contribution to the reflected intensity, with a resulting dilution of the opposition effect and change in shape of the phase curve. Let us compute the magnitude of this effect.

Apart from the shadowing effect, the intensity reflected by Saturn's rings will satisfy the equation of radiative transfer

$$\mu \frac{dI}{d\zeta} = -I + \frac{a}{4\pi} \int_{4\pi} d\Omega' \Phi(\Omega, \Omega') I(\Omega') \quad (9)$$

where a and Φ have been defined above. Since the optical thickness of the rings is not large, it is convenient to express the solution to equation (9) as the sum of successive orders of scattering (van de Hulst, 1948; van de Hulst and Irvine, 1963; Irvine, 1964), so that

$$I(\Omega, \zeta) = \sum_{n=0}^{\infty} a^n I_n(\Omega, \zeta) \quad (10)$$

where I_n is the n -th order scattering intensity for $a = 1.0$. Since we take the optical thickness of the rings as known in the computation of a particular model, equation (10) provides an efficient means for determining the effect of a change in particle albedo. The desired ring reflectivity including the shadowing effect is thus, from equations (1), (6), and (10),

$$R(\Omega) = R_1^S(\Omega) + I(\Omega, 0) - aI_1(\Omega, 0) \quad (\mu > 0) . \quad (11)$$

The ring reflectivity will be a function of the parameters a , τ , Ω_0 , and D , as well as direction Ω and the properties of the phase function Φ .

The successive terms in equation (10) are found, for incident flux π through the horizontal upper boundary of the rings, from the relations

$$I_0(\Omega, \zeta) = \frac{\pi F' \delta(\mu - \mu_0) \delta(\phi - \phi_0) e^{-\zeta/\mu_0}}{\mu_0}$$

$$B_n(\Omega, \zeta) = \frac{1}{4\pi} \int_0^{2\pi} d\phi' \int_{-1}^1 d\mu' \Phi(\Omega, \Omega') I_{n-1}(\Omega', \zeta)$$

$$I_n^+(\Omega, \zeta) = \int_{\zeta}^{\tau} d\zeta' e^{-(\zeta' - \zeta)/\mu} \frac{B_n}{\mu}(\Omega, \zeta') \quad (12)$$

$$I_n^-(\Omega, \zeta) = \int_0^{\zeta} d\zeta' \left(-\frac{1}{\mu}\right) e^{-(\zeta' - \zeta)/\mu} B_n(\Omega, \zeta')$$

$$I_n(\theta = \pi/2, \phi, \zeta) = B_n(\theta = \pi/2, \phi, \zeta)$$

where B_n is the so-called source function for n th order scattering, $\delta(x)$ is the Dirac delta function, and the superscripts + and - refer to the cases $\theta < \pi/2$ and $\theta > \pi/2$, respectively. As has been emphasized in the above references, the ratio of successive term I_n/I_{n-1} approaches a constant value as n increases, so that the series (10) may be truncated and the remainder replaced by a geometric series.

The double integrations over θ and ϕ in the above equations may be eliminated by expanding the phase function in a cosine series in $(\phi - \phi_0)$ (e.g., Hansen, 1969). Setting

$$\phi(\mu, \phi; \mu, \phi_0) = \sum_{m=0}^{\infty} \Phi^m(\mu, \mu_0) \cos m(\phi - \phi_0) \quad (13)$$

we have

$$B_n(\mu, \phi, \zeta; \mu_0, \phi_0) = \sum_{m=0}^{\infty} B_n^m(\mu, \zeta; \mu_0) \cos m(\phi - \phi_0)$$

$$I_n^+(\mu, \phi, \zeta; \mu_0, \phi_0) = \sum_{m=0}^{\infty} I_n^{m+}(\mu, \zeta; \mu_0) \cos m(\phi - \phi_0) \quad (14)$$

$$I_n^-(\mu, \phi, \zeta; \mu_0, \phi_0) = \sum_{m=0}^{\infty} I_n^{m-}(\mu, \zeta; \mu_0) \cos m(\phi - \phi_0)$$

where

$$B_1^m = \frac{1}{4\mu_0} e^{-\zeta/\mu_0} \Phi^m(\mu, \mu_0)$$

$$B_n^m = \frac{1}{(4 - 2\delta_{0,m})} \int_{-1}^1 d\mu' \Phi^m(\mu, \mu') I_{n-1}^m(\zeta, \mu', \mu_0) \quad (15)$$

$$I_n^{m+}(\mu, \zeta, \mu_0) = \int_{\zeta}^{\tau} \frac{d\zeta'}{\mu} e^{-(\zeta' - \zeta)/\mu} B_n^m(\mu, \zeta', \mu_0)$$

$$I_n^{m-}(\mu, \zeta, \mu_0) = \int_0^{\zeta} \frac{d\zeta'}{-\mu} e^{-(\zeta' - \zeta)/\mu} B_n^m(\mu, \zeta', \mu_0)$$

Since the ring particle phase function is not known a priori, we shall choose a simple analytic expression which may be parameterized to conveniently describe a wide variety of phase functions. Such a

function, which is also easily expressed in the form of equation (13), is the Henyey-Greenstein function

$$\Phi_{\text{HG}}(\gamma, g) = \frac{(1 - g^2)}{(1 + g^2 - 2g \cos \gamma)^{3/2}} \quad (16)$$

where

$$g = \frac{1}{2} \int_{-1}^1 d\mu \mu \Phi_{\text{HG}}(\mu) \quad (17)$$

and γ is the scattering angle. The parameter g , called the asymmetry factor of the phase function, satisfies $-1 \leq g \leq 1$ and characterizes the elongation of the phase function in a polar diagram. For $g = 0$, the scattering is isotropic; for $g > 0$, photons are scattered primarily in the forward direction; and for $g < 0$, photons are scattered primarily in the backward direction.

We note that

$$\Phi_{\text{HG}}(\gamma, g) = \sum_{n=0}^{\infty} (2n + 1) g^n P_n(\cos \gamma) \quad (18)$$

where

$$\cos \gamma = \mu \mu_0 + \sqrt{1 - \mu^2} \sqrt{1 - \mu_0^2} \cos(\phi - \phi_0)$$

and P_n and P_n^m are the Legendre and the associate Legendre polynomials, respectively. Using the addition theorem we thus obtain

$$\Phi_{HG}(\gamma, g) = 1 + \sum_{n=1}^{\infty} (2n+1) g^n [P_n(\mu) P_n(\mu_0) + 2 \sum_{m=1}^n \frac{(n-m)!}{(n+m)!} P_n^m(\mu) P_n^m(\mu_0) \cos m(\phi - \phi_0)] \quad (19)$$

which may be written

$$\Phi_{HG}(\gamma, g) = \sum_{\kappa=0}^{\infty} \Phi_{HG}^{\kappa}(\mu, \mu_0, g) \cos \kappa(\phi - \phi_0) \quad (20)$$

where

$$\Phi_{HG}^0(\mu, \mu_0, g) = 1 + \sum_{n=1}^{\infty} (2n+1) g^n P_n(\mu) P_n(\mu_0) \quad (21)$$

$$\Phi_{HG}^{\kappa}(\mu, \mu_0, g) = 2 \sum_{n=\kappa}^{\infty} (2n+1) g^n \frac{(n-\kappa)!}{(n+\kappa)!} P_n^{\kappa}(\mu) P_n^{\kappa}(\mu_0), \quad \kappa \neq 0 .$$

In our models for this paper we shall use the phase function

$$\Phi(\gamma) = b \Phi_{HG}(\gamma, g_1) + (1 - b) \Phi_{HG}(\gamma, g_2) \quad (22)$$

which is normalized such that

$$\frac{1}{2} \int_0^{\pi} d\gamma \sin \gamma \Phi(\gamma) = 1 \quad (23)$$

Equation (22) allows us to investigate particle phase functions which are isotropic, principally forward directed, principally backward directed, or which contain both a forward and backward peak. The parameter b satisfies $0 \leq b \leq 1$.

S E C T I O N I V

COMPARISON WITH THE OBSERVATIONS

Using the results of the previous section we may write for the theoretically predicted phase curve $M(\alpha)$ in stellar magnitudes

$$M(\alpha) = -2.5 \log \left[\frac{\langle R_1^S(\alpha) \rangle + \sum_{n=2}^{\infty} R_n(\alpha)}{\langle R_1^S(0) \rangle + \sum_{n=2}^{\infty} R_n(0)} \right] \quad (24)$$

where we write $R_n = a^n I_n(\zeta = 0)$ and the angular brackets denote an integration of the incident radiation over the disk of the sun. In order to illustrate more clearly the role of the parameters involved, we may use equation (3) to rewrite equation (24) as

$$M(\alpha) = -2.5 \log \left[\frac{a \Phi(\pi - \alpha) \langle S(\alpha) \rangle + \sum_{n=2}^{\infty} R_n(\alpha)}{a \Phi(\pi) \langle S(0) \rangle + \sum_{n=2}^{\infty} R_n(0)} \right] \quad (25)$$

where

$$\langle S(\alpha) \rangle \equiv \left\langle \frac{1}{4\mu\mu_0} \int_0^{\tau} d\zeta' \exp\left[-\zeta' \left(\frac{1}{\mu} + \frac{1}{\mu_0}\right) + nC(\alpha)\right] \right\rangle \quad (26)$$

is the primary scattered intensity including the shadowing effect for the case of conservative ($a = 1.0$), isotropic scattering.

Equation (25) may be further transformed to simplify the

comparison with the observations. Because the higher order scattering component of the intensity does not change rapidly with angle and because the maximum phase angle observable for Saturn is 6° , we will have to

$$\sum_{n=2}^{\infty} R_n(0) \simeq \sum_{n=2}^{\infty} R_n(\alpha) \quad (27)$$

In fact, for the cases investigated below, equation (27) holds to better than one percent. It is then convenient to rewrite equation (25) as

$$M(\alpha) = -2.5 \log \left[\frac{\frac{\phi(\pi - \alpha)}{\phi(\pi)} \frac{\langle S(\alpha) \rangle}{\langle S(0) \rangle} + x}{1 + x} \right] \quad (28)$$

where

$$x \equiv \frac{\sum_{n=2}^{\infty} R_n(0)}{a \phi(\pi) \langle S(0) \rangle} \quad (29)$$

is the ratio of the reflected intensity due to higher order scattering to the reflected intensity due to primary scattering including the shadowing correction, while the other ratio in the numerator of equation (28) is the intensity ratio which appeared in the definition of $\delta M(D)$ according to equation (8). We thus see that the shape of the phase curve will depend on the quantities x , the phase function ϕ , and the optical thickness τ and volume density D through $\langle S \rangle$. The single scattering albedo a enters indirectly through x . It is these parameters D , τ , a , and the quantities characterizing the phase function which we wish to determine. From them, we may hope

to further deduce the nature of the ring particles.

In addition to the phase curve, the absolute surface brightness of ring B at opposition is a critical measurement for defining the ring parameters. Noting that the incident flux on the rings will be $\pi F \mu_o$, where πF is the solar flux at the distance of Saturn through an area normal to the direction to the sun, we may related the observed absolute brightness at opposition to that intensity $R^o \equiv R(\alpha = 0)$ calculated from equation (11) by the normalization factor $F\mu_o$ to obtain

$$R^o = \frac{\pi I_R}{\pi F \mu_o} \frac{I_D}{I_D} = \frac{1}{\mu_o} \frac{I_R}{I_D} \frac{I_D / \pi F}{(1/\pi)}$$

$$R^o = \frac{1}{\mu_o} P_S \frac{I_R}{I_D} \tag{30}$$

where I_D is the mean specific intensity averaged over Saturn's disk, I_R is the mean specific intensity of the ring B, and P_S is the geometric albedo of Saturn's disk. The geometric albedo is the ratio of the mean brightness of the planetary disk at full phase to the brightness of an intrinsically white screen of the same diameter as the planet, located at the same point perpendicular to the sunlight. If the brightness of the surface is the same in all directions, this requires energy reflected in a given direction θ by any surface element to be proportional to $\cos\theta$. This is known as Lambert's cosine law. A reflective surface which obeys this law is called a Lambert surface. If such a surface reflects all the incident light it is said to be an

intrinsically white surface. Using the data of Cook, Franklin, and Palluconi (1973) for I_R/I_D and the value $P_S = 0.429$ for V from Irvine and Lane (1973), we find a value in the visual of $R_V^O \approx 1.2$. Because the disk was partly shielded by the rings during the Franklin and Cook observations, this value of R_V^O is based on an I_D which will be biased towards Saturn's equatorial regions.

We may obtain an independent estimate of the brightness of ring B by multiplying the corresponding data of Price (1973), which apply to the total ring system, by a factor of 1.2, which is the correction determined from Franklin and Cook necessary to transform to ring B alone. The corrected Price data give $R_V^O = 1.1 \pm 0.1$ at a ring inclination of 64° , which is appropriate to the present discussion.

The wavelength dependence of the surface brightness is of critical importance in determining the ring parameters. The principal data relevant to this problem are the observations in B and V of Franklin and Cook (1965), the relative spectral reflectivity measurements of ring B by Lebofsky et al. (1970), the similar data from Irvine and Lane (1973) which were deduced from observations of the combined light of the Saturn system, and some recent spectral scans by Kharitonova and Teifel (1973). The data are in reasonable agreement for $\lambda \leq 0.6\mu$ if we bear in mind the color dependence of the opposition effect as reported by Franklin and Cook and Irvine and Lane. At longer wavelengths, however, there are some serious disagreements. The ring reflectivity for $\lambda > 0.6\mu$ increases slowly with increasing λ in the results of Lebofsky et al., while Irvine and Lane's results indicate

that the reflectivity has a peak in the wavelength range from 0.6μ to 0.8μ and declines sharply with increasing λ from 0.8μ to 1.1μ . (See Figure 5.)

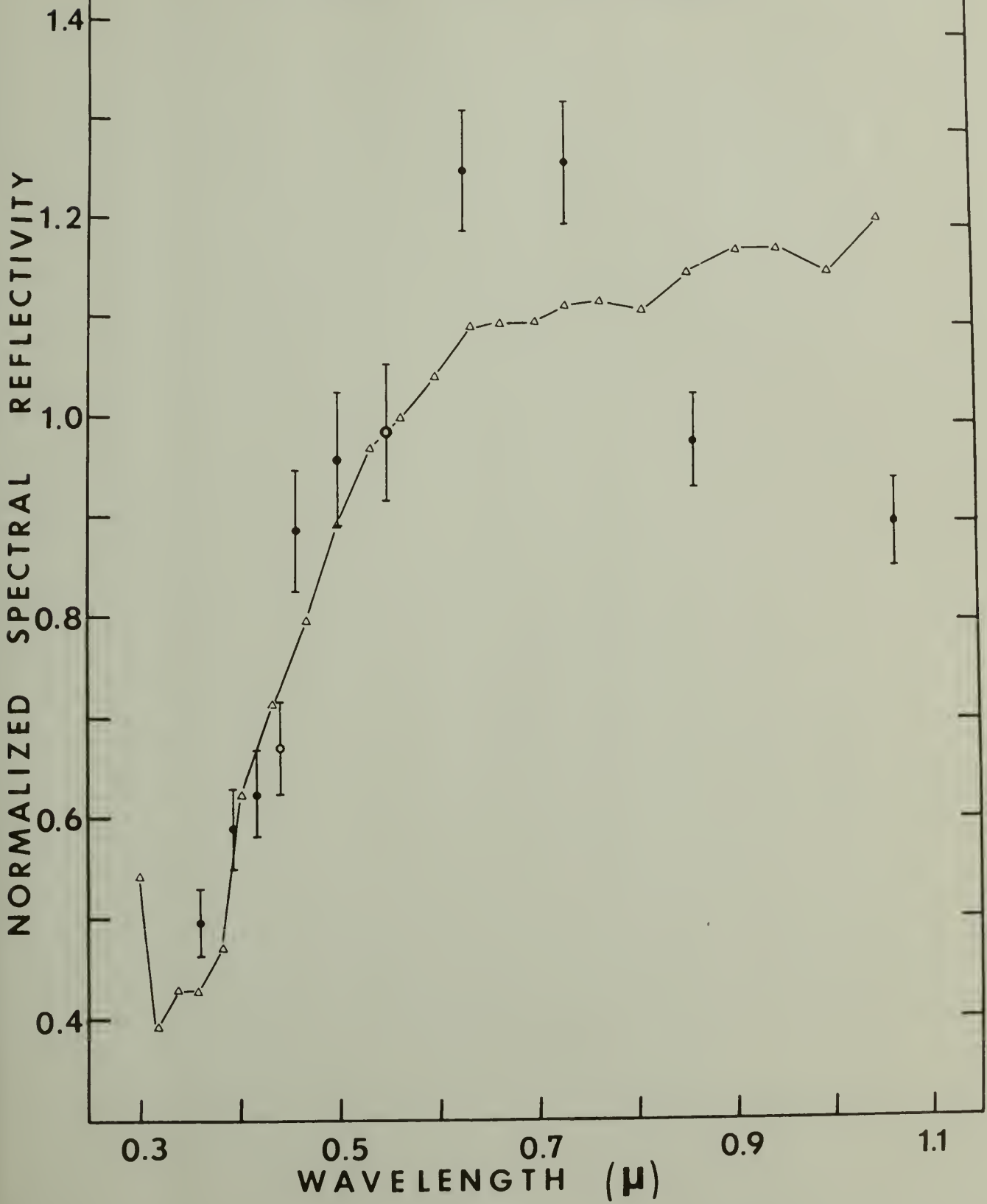
Since these reflectivity observations were made at different declination angles of the sun relative to the ring plane, this factor was examined. We calculated the brightness of the ring in the red R_R and the brightness in the visual R_V at three different declination angles (64° , 72° , and 83°) from equation (10). We assumed $a_R = 1.0$, $a_V = 0.9$ and a wavelength-independent particle phase function similar to the phase function (4) which is defined later in this section and is shown in Figure 8. We found that the ratio of R_R/R_V at all three different angles is ~ 1.2 and is insensitive to the change of angle. The possibility that the difference in the declination angle of the sun causes the different observational results is, therefore, unlikely.

The big disagreement among the spectral data for $\lambda > 0.6\mu$ might reflect the uncertainty in separating ring and disk brightness in the Irvine and Lane observations, or actual temporal variations due perhaps to differences in the insolation (changing distance of Saturn from the sun), or differences in the brightness of the rings on the East and West side, as has been reported consistently back through the literature. Although the recent spectral data by Kharitonova and Teifel ($0.35\mu < \lambda < 0.8\mu$) indicate high reflectivity in the red similar to the results of Irvine and Lane, further homogeneous data on this subject are necessary to solve this mystery.

We shall limit ourselves for the present to the observations by

Figure 5: Spectral reflectivity of Saturn's rings normalized to unity at the visual wavelength ($\lambda = 0.564\mu$) and excluding the opposition effect. Connected points from Lebofsky et al. (1970). Broad (open circles) and narrow band (closed circles) data with error bars from Irvine and Lane (1973).

RINGS OF SATURN



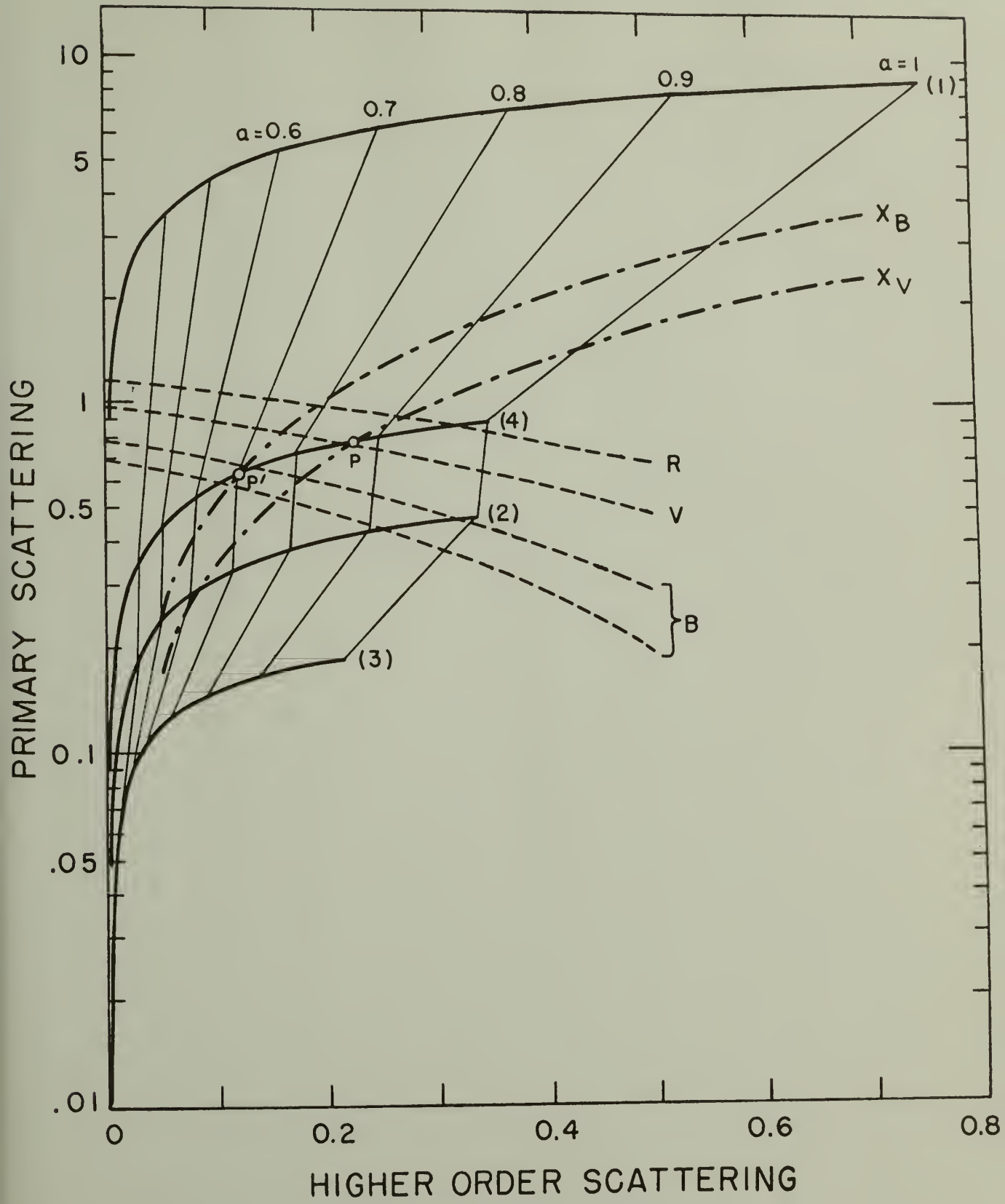
Lebofsky et al. as the most direct and completely reported results at this time. Using their data to scale the visual reflectivity, we obtain in the B band $R_B^O \sim 0.83$ and a maximum value near 1 micron of $R_R^O \sim 1.3$. These data do not include a differential opposition effect. Since the differential opposition effect between the blue and the visual is approximately 5% (Franklin and Cook, 1965; Irvine and Lane, 1973), we shall take $R_B^O \sim 0.87$. We shall for the present neglect any differential opposition effect between the visual and the red, in spite of the indication for such an effect from Irvine and Lane. We return to these questions in Section VI below.

We wish our theoretical model to match both the absolute brightness measurements and the shape of the phase curves in B and V. We may facilitate this comparison by considering the diagram in Figure 6. The vertical axis represents the primary scattered radiation, including the shadowing effect, computed at $\alpha = 0.094^\circ$. This will be given theoretically by a $\Phi(\pi - 0.094^\circ) < S(\alpha = 0.094^\circ) >$, where we recall that this value of α is the minimum obtained during the observations of Franklin and Cook. The horizontal axis in Figure 6 represents the sum of the higher order scattering, which according to the model is $\sum_2^n R_n$. The dashed curves designated R, V and B are the loci of points which satisfy the observed absolute brightness in the red, visual, and blue, respectively. For agreement with the model the absolute brightness must be

$$R(\alpha = 0.094^\circ) = a \Phi(\pi - 0.094^\circ) < S(\alpha = 0.094^\circ) > + \sum_{n=2}^{\infty} R_n(a, \Phi) \quad (31)$$

Figure 6: Diagram for comparison of observation and theory.

Vertical axis gives primary scattering contribution to total brightness, horizontal axis gives multiple scattering contribution. Dashed lines are loci of points with observed total brightness for the red (R), visual (V), and blue (B), respectively. Dash-dot lines are loci of points with correct ratio x of primary to higher order scattering to match shape of phase curve in $V(x_V)$ and $B(x_B)$, respectively. Solid lines are theoretical computations of total brightness for the phase functions (1), (2), (3) and (4) shown in Figure 8. The particle albedo is a .



where the indicated arguments draw attention to the dependence of the quantities on phase angle α and phase function Φ . We have plotted as an example the lower observational limits of the absolute surface brightness $R_V^O = 1.0$ and $R_R^O = 1.2$ in V and R, respectively, and have shown an uncertainty of ± 0.05 for B as an example of the possible uncertainty in these measurements. In fact, these lower limits on the observed brightness allow the largest possible range of particle albedo a in the comparison with theory, and also lead to a lower limit on the volume density D .

For given D and τ , the shape of the phase curve $M(\alpha)$ for $1^\circ < \alpha < 2^\circ$ and for $\alpha \geq 2^\circ$ depends principally upon the parameter of multiple scattering x and upon the phase function Φ , respectively. By experimenting with a wide choice of values for these parameters and also for the phase function Φ , we find that the sharp peak in the opposition effect ($\alpha \leq 1^\circ$) depends primarily upon the value of D , and that the observations restrict D to a narrow range around the value 0.01. Let us for the present take $\tau = 1$ on the basis of the observations of stellar occultations by the ring discussed by Cook, Franklin, and Palluconi (1973). Since from equation (28) only the relative shape of the phase function near 180° is important in producing the linear increasing portion of the phase curve, we may use $\Phi_{HG}(\pi - \alpha, g) / \Phi_{HG}(\pi, g)$ instead of $\Phi(\pi - \alpha) / \Phi(\pi)$. By doing that, g will be the dummy parameter which represents the effect of the phase function in the calculation of the theoretical phase curve. The real phase function $\Phi(b, g_1, g_2)$ will be found after the analysis of the absolute brightness data. For example, for $D = 0.01$, the appropriate value of g is about -0.67 and

those of x are 0.29 and 0.17 in V and B, respectively. We then list in Table I values of x and g for several choices of D which produce theoretical phase curves which agree with the observations in B and V. The dash-dot curves plotted in Figure 6 are now the loci of points for which the fraction of multiple scattering is $x_B = 0.17$ and $x_V = 0.29$, respectively. The corresponding phase curves are shown in Figure 7.

We may now use Figure 6 to determine the single scattering albedo a and properties of the phase function for the ring particles if we assume that the differences in brightness and phase curve for B and V result only from a change in particle albedo a . In other words, we assume that as the albedo of the particles changes with wavelength, the relative angular distribution of scattered light remains unchanged. This is a reasonable approximation for large, bright particles (which are necessary to produce the shadowing effect and the observed high ring brightness) for which geometrical optics is valid. Our whole approach to the shadowing effect through geometrical optics also requires that τ be independent of wavelength. If we now call the intersection between the curves V and x_V in Figure 6 a point P, and the intersection between the middle of the range B and the curve x_B a point P', then the theoretically computed brightness curve for the rings which passes through both the points P and P' will match the observed absolute brightness and also the observed phase curves. We have plotted in Figure 6 such theoretical brightness curves for four different phase functions obtained from equation (22). We have taken the center of the sun and earth in directions corresponding to the

Table I: Allowable range of parameters such as volume density D , multiple scattering contribution x , asymmetry factor g of Henyey - Greenstein phase function, ring particle albedo a for $\tau = 1$ is shown.

TABLE I

Multiple Scattering Contribution x and
Phase Function Asymmetry g for $\tau = 1$

Volume density, D	Multiple scattering, x	g
$D = 0.012$		
B	0.14 ± 0.02	-0.64 ± 0.02
V	0.26 ± 0.02	
$D = 0.010$		
B	0.17 ± 0.02	-0.67 ± 0.02
V	0.29 ± 0.02	
$D = 0.008$		
B	0.22 ± 0.02	-0.72 ± 0.01
V	0.34 ± 0.02	

Allowable Range of Parameters

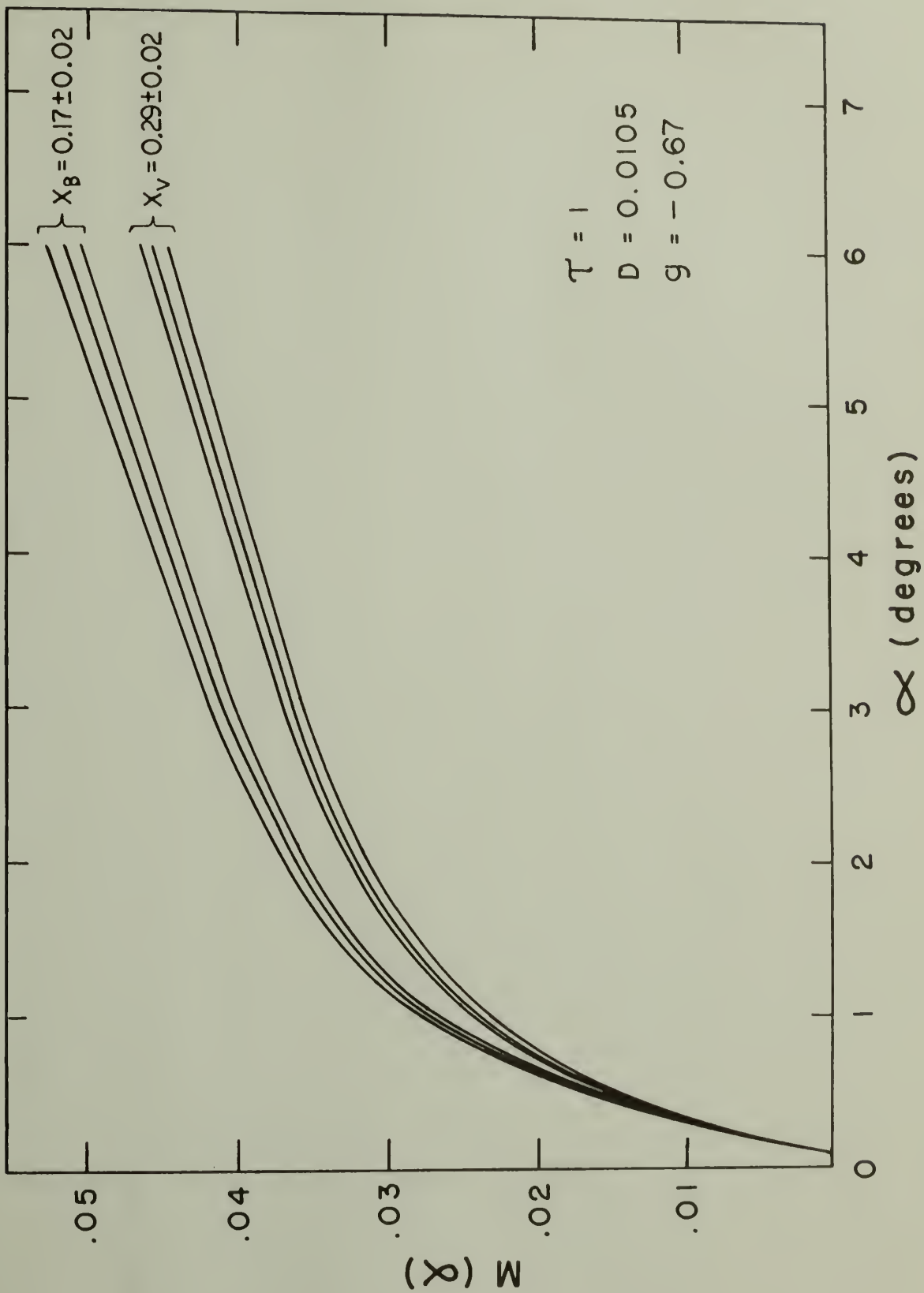
Monodisperse Case for $\tau = 1$

$$0.008 \leq D \leq 0.012$$

$$0.65 \leq a_B \leq 0.75$$

$$0.82 \leq a_V \leq 0.9$$

Figure 7: Theoretical phase curves for ring optical thickness $\tau = 1.0$ which match the observations of Franklin and Cook (1965). Parameters of multiple scattering are x_B and x_V in B and V, respectively. Asymmetry factor of Henyey - Greenstein phase function is g . Volume density is D .



Franklin and Cook observations. The solid lines represent such brightness curves for the phase functions (1) $b = 0$, $g_1 = 0$, $g_2 = -0.7$ (a very strong backward peak with no forward scattering); (2) $b = 1$, $g_1 = 0$, $g_2 = 0$ (isotropic scattering); (3) $b = 0.988$, $g_1 = 0.7$, $g_2 = -0.805$ (a very strong forward peak with a small backward peak, reminiscent of the phase function for terrestrial clouds); (4) $b = 0.995$, $g_1 = -0.14$, $g_2 = -0.84$ (a more slowly varying backward scattering phase function with a slight peak near 180°). These phase functions are illustrated in Figure 8. All of them except (2), isotropic scattering, have a similar slope near 180° which produces a roughly satisfactory shape to the phase curve in the linearly varying region. The albedo a is the only variable unspecified in the theoretical brightness curves in Figure 6, and it thus serves as a parameter whose variation along the curves is indicated.

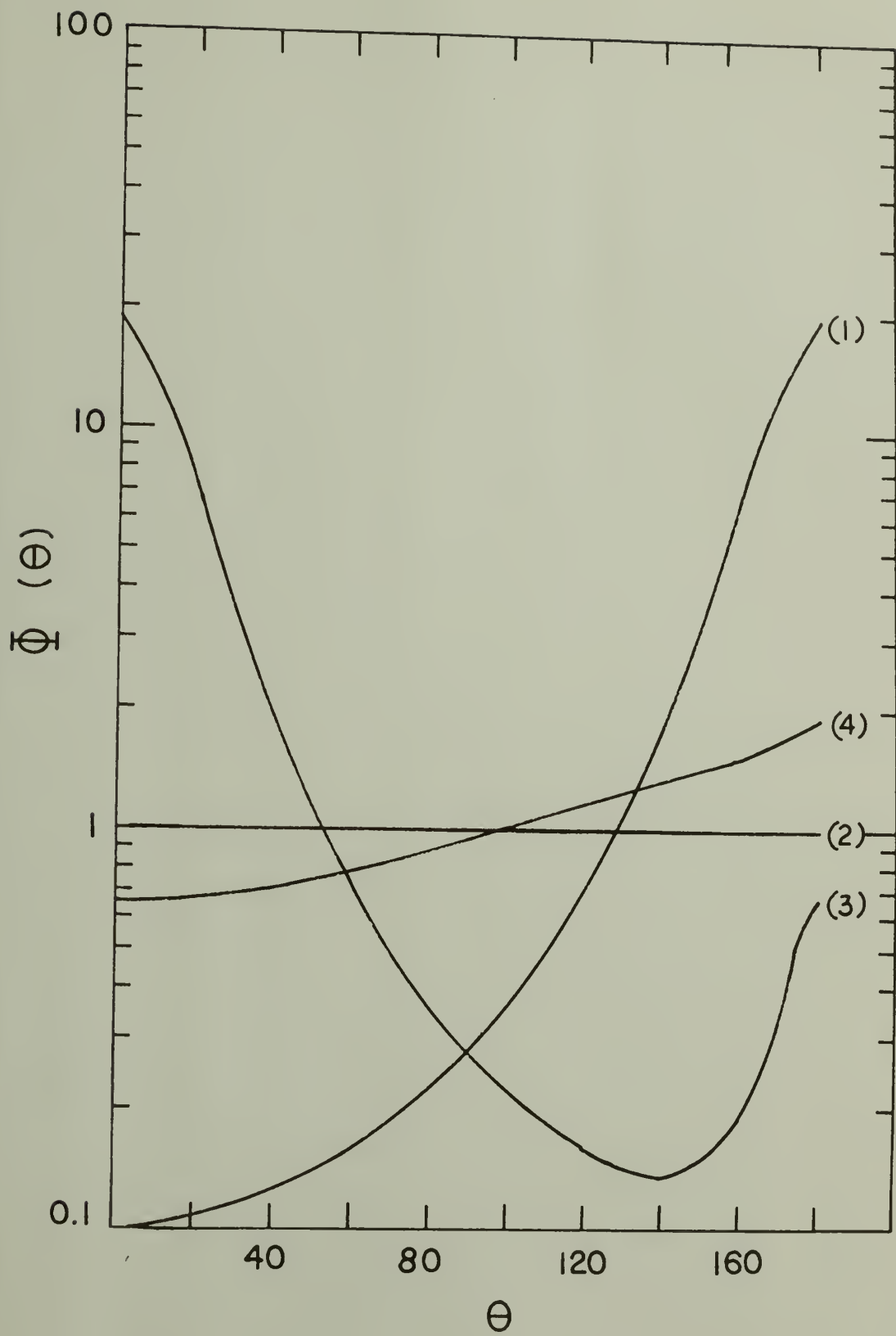
The power of this procedure is illustrated by the large differences between the curves (1-4) in Figure 6. The requirement that the model match both the shape of the phase curve and the absolute brightness clearly puts significant restrictions on the form of the phase function. In particular, it is quite evident that neither the phase function with a very strong backward peak nor that with a very strong forward peak can match the observations. Some degree of back-scattering is required to match the phase curve, so that the phase curve must be similar in shape to the curve (4). Although the shape of the phase curve (apart from the opposition peak) depends principally on the values of ϕ near 180° (corresponding to the small phase

angles observable for Saturn), an appropriate phase function cannot be very different from the curve (4). If it decreased much more sharply with decreasing $\theta = \pi - \alpha$, it will not satisfy the normalization condition. The addition of a shallow forward peak to the phase function would be possible and would require a lower backward peak; that is, the phase function would become more isotropic.

We may now determine the single scattering albedo from the position of the points P and P' on the curve (4) in Figure 6. We find $a_V = 0.87$ and $a_B = 0.70$. By normalizing the phase function (4) to unity at $\alpha = 180^\circ$ and integrating, we may obtain the phase integral q for the ring particles as $q = 2.1$. The resulting geometric albedos in the visual and blue for the ring particles are then $p_V = a_V/q = 0.41$ and $p_B = 0.33$.

Figure 8: Four sample phase functions ϕ (see equation 22) used for the calculations illustrated in Figure 6.

- (1) $b = 0$, $g_1 = 0$, $g_2 = -0.7$ (a very strong backward peak with no forward scattering).
- (2) $b = 1$, $g_1 = 0$, $g_2 = 0$ (isotropic scattering).
- (3) $b = 0.988$, $g_1 = 0.7$, $g_2 = -0.805$ (a very strong forward peak with a small backward peak, reminiscent of the phase function for terrestrial cloud).
- (4) $b = 0.995$, $g_1 = -0.14$, $g_2 = -0.84$ (a more slowly varying backward scattering phase function with a slight peak near 180°).



S E C T I O N V

ALLOWABLE RANGE OF PARAMETERS

As a result, we may say that a satisfactory model of the B ring which matches the observed phase curves in B and V and also the corresponding absolute brightnesses has optical thickness $\tau = 1$, a volume density $D = 0.010$, and ring particles with a phase function given by (4) in Figure 8 and Bond albedos of $a_V = 0.87$ and $a_B = 0.70$. We can also estimate the albedos in UV and R by scaling the reflectivity measurements of Lebofsky et al. (1970). We find this way $a_{UV} = 0.45$ and $a_R = 0.96$.

It is of course important to see how much each of these parameters can be varied without disrupting the fit of the model to the data. Because the parameters cannot be varied independently if the model is going to continue to match the observations, the problem is difficult. Some possible directions in which changes may occur are sketched below.

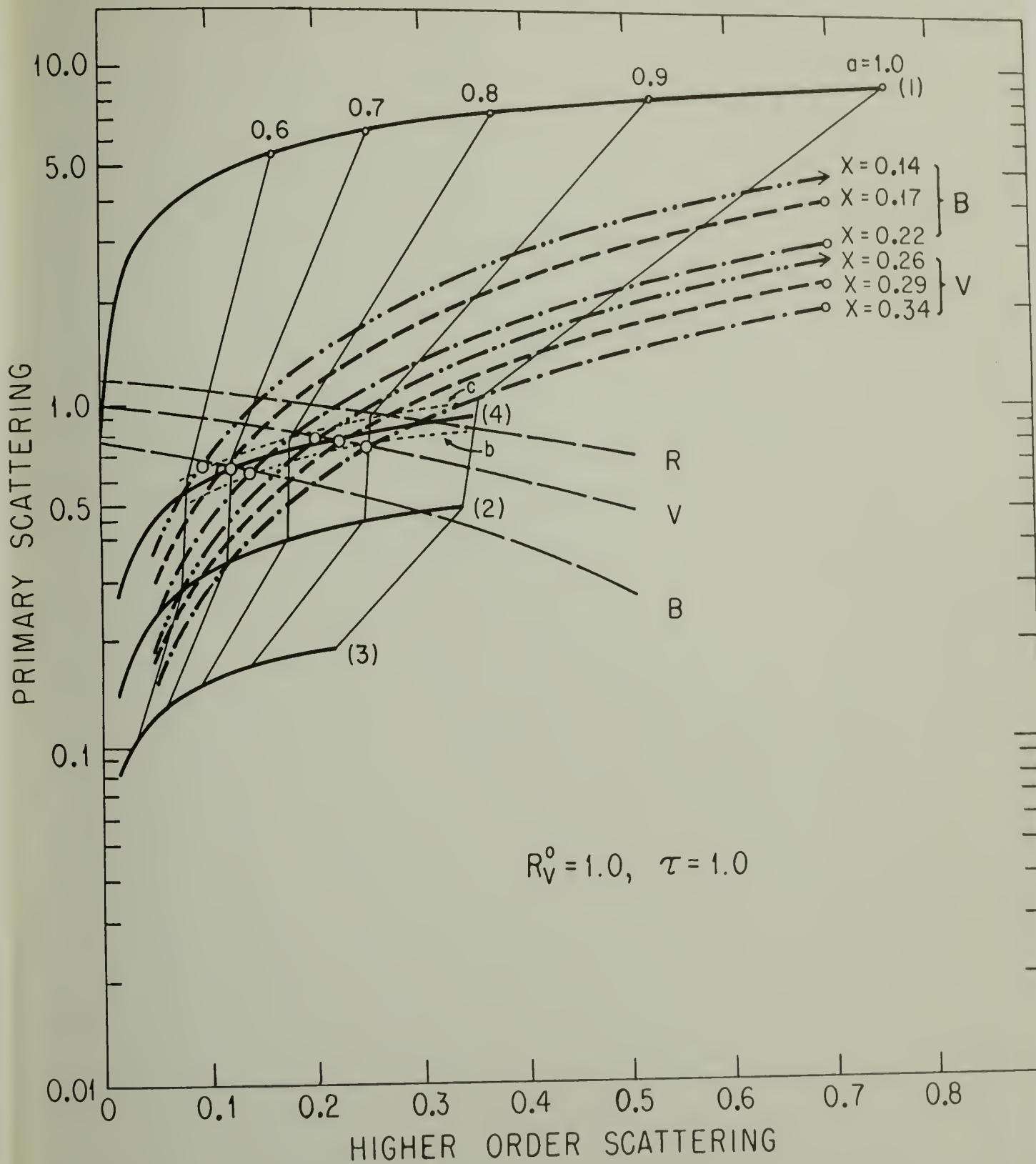
If the optical thickness τ of the layer is kept constant at a value of unity, the value of D can be reduced only slightly from that discussed above. When $D = 0.008$, computations (whose results are shown in Table I) indicate that the multiple scattering contributions x needed to match the phase curves are $x_B = 0.22$ in B and $x_V = 0.34$ in V. Since from Figure 6, all the theoretical brightness curves are quite similar in shape, the appropriate theoretical brightness curve for the present case will be quite similar to the brightness curve (4) except that it will pass through the new points p' and p for the case $D = 0.008$.

Such a curve is shown as the broken line b in Figure 9. The corresponding phase function in this case will be slightly less backward scattering than the phase function (4). As is seen from Figure 9, the broken line b crosses the dashed curve R when the particle albedo in the red $a_R \sim 1.0$. In other words, lowering of D must be compensated by an increase in multiple scattering which requires an increase in the particle albedo in V and B, and a resulting increase in the particle albedo for R also. But $a_R \leq 1$ on physical grounds, so that the brightness of the rings in the red could not be matched by the model if $D < 0.008$. It might be expected from Figure 3 that reduction of D to a value less than 0.005 would begin to reduce the shadowing effect. This is in fact true, but the resulting shape of the phase curve near $\alpha = 0$ is too steep to agree with the observations.

As has been pointed out in a previous section, if the value of D is too large, the opposition peak will be too broad. For the present choice of the other parameters the upper limit on D is approximately 0.012. With this value we obtain multiple scattering contributions x of 0.26 in V and 0.14 in B. The corresponding values of albedo parameterizing the theoretical brightness curve are $a_V \approx 0.82$ and $a_B \approx 0.65$ from the broken line C (drawn in a manner of analogous to the broken line b described above) in Figure 9. The phase function in this case will be slightly more backward scattering than the phase function (4).

The above results for $\tau = 1$ and the minimum surface brightness allowed by the observations are summarized in Table I, including the

Figure 9: Diagram for comparison of observation and theory for $\tau = 1$ and $R_V^0 = 1.0$ showing the allowable range of albedos. Same notation as Figure 6. The broken lines b and c are described in text.



admissible range of the particle albedos in B and V.

We have also examined the case $\tau = 0.7$ as an estimate of the effects of this possible lower limit for ring B. We find that a somewhat smaller value of $D \sim 0.006$ is required to match the shape of the opposition peak. The magnitude of the shadowing effect due to single scattering decreases with decreasing τ , but this may be compensated by decreasing the dilution of the shadowing effect due to multiple scattering. In the present case we find it necessary to take approximately $x_V \approx 0.21$ and $x_B \approx 0.10$, as illustrated in Figure 10. Constructing Figure 11 analogous to Figure 6 for the present case we find that a somewhat more backscattering phase function is required, although in general its shape will be similar to that for the case $\tau = 1$. In constructing Figure 11, we have not carried out the complete numerical computation for the theoretical brightness curve passing through the points p' and p for $\tau = 0.7$. The broken line in Figure 11 is drawn such that it has a similar shape of the theoretical brightness curve for the isotropic phase function (solid line in Figure 11) and also passes the new points p' and p for the case $\tau = 0.7$ and $D = 0.006$.

The appropriate theoretical brightness curve in this case will be quite similar to the broken line in Figure 11. This argument can be justified when we go back to Figure 9. In Figure 9 the theoretical brightness curve (4) has a quite similar shape of the theoretical brightness curve (2) for the isotropic phase function in the flattened part of the curve. The corresponding albedo range is estimated to be $0.6 \lesssim a_B \lesssim 0.7$ and $0.85 \lesssim a_V \lesssim 0.9$ from comparison of Figures 9 and 11, which are not drastically different from their values for $\tau = 1$. In

Figure 10: Theoretical phase curves for $\tau = 0.7$ which match the observations. Same notation as Figure 7. Compare with Figure 7, for $\tau = 1$.

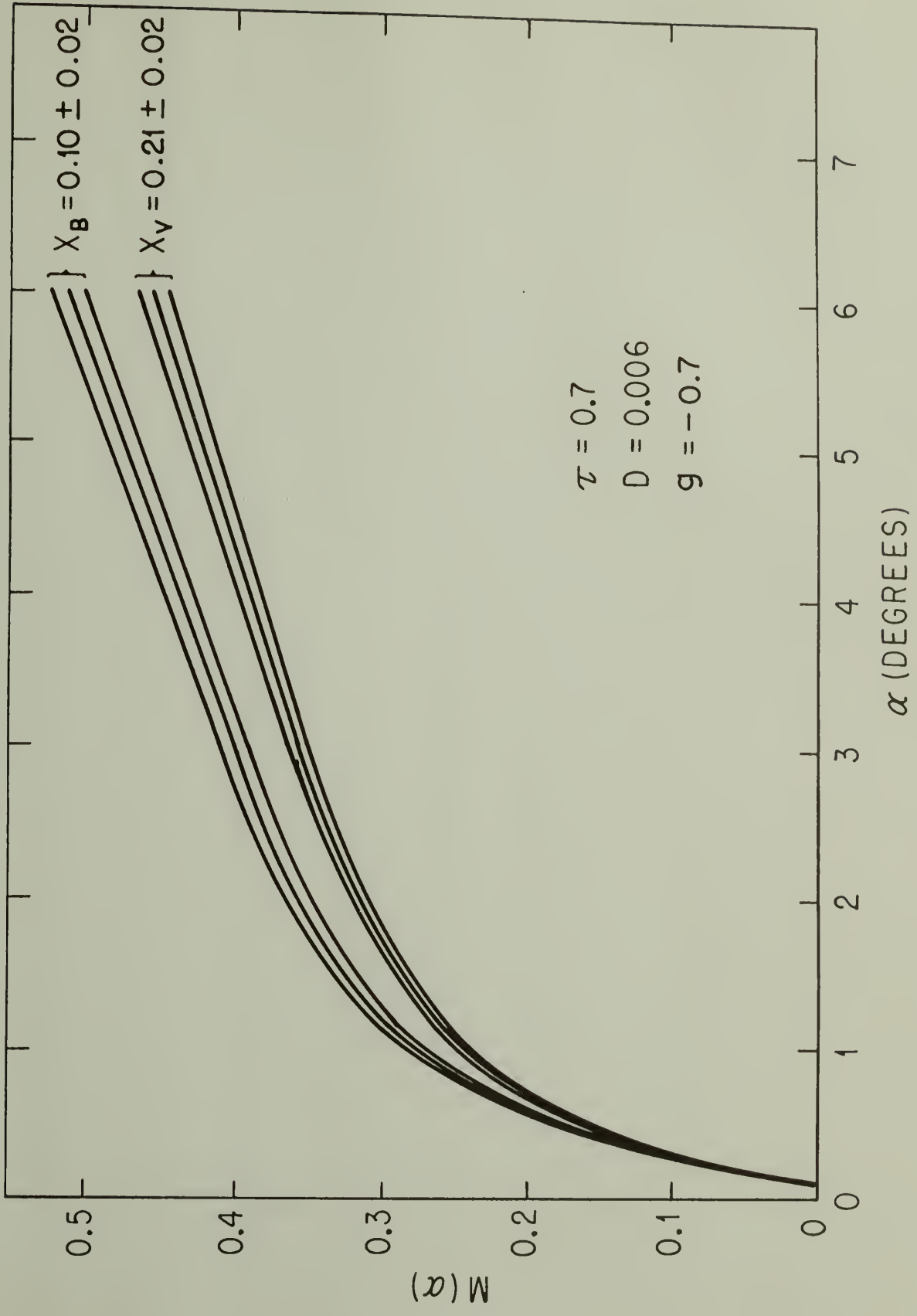
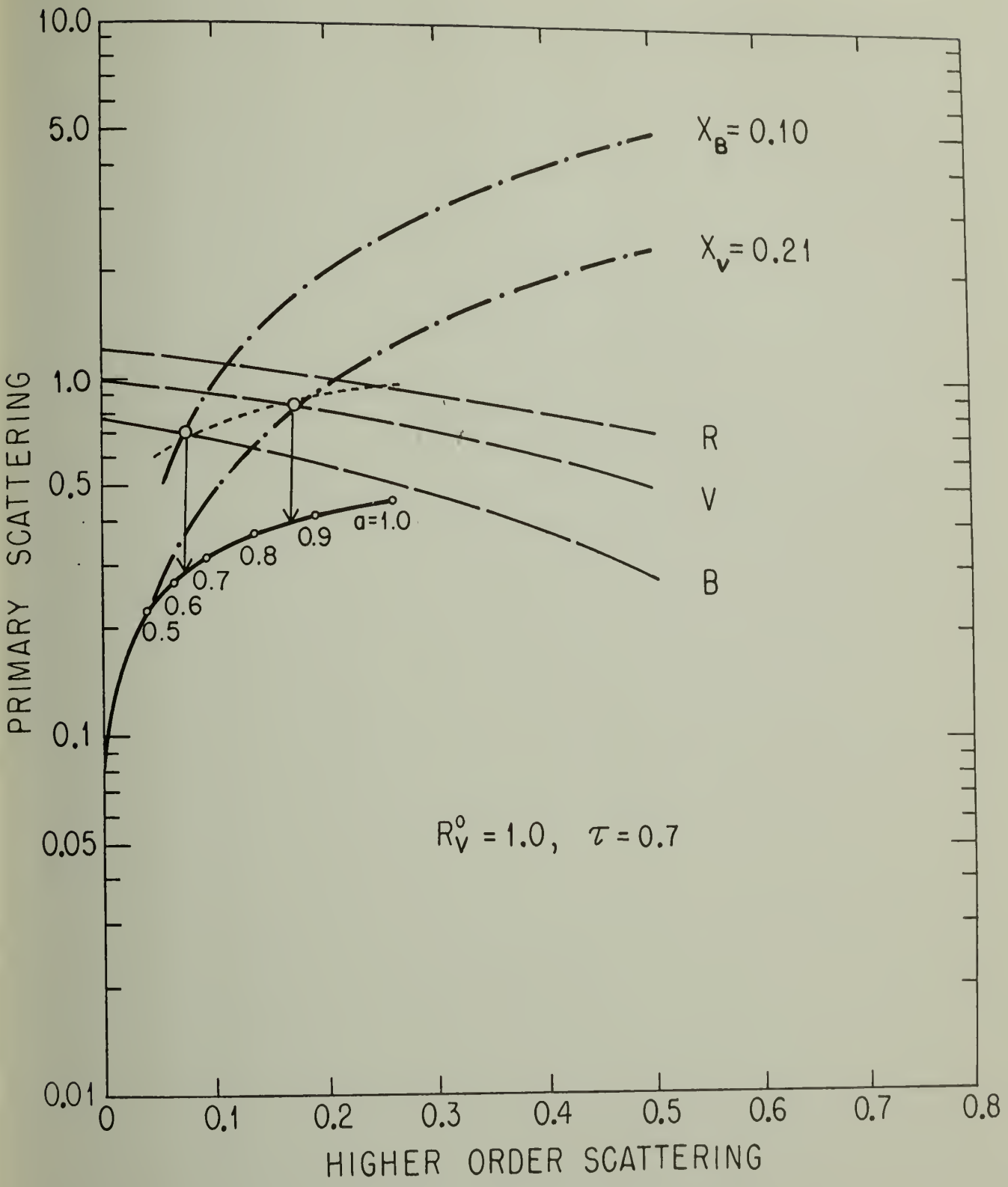


Figure 11: Diagram for comparison of observation and theory for $\tau = 0.7$ and $R_V^0 = 1.0$. Same notation as Figure 6. Theoretical brightness curve is for an isotropic phase function (solid line). The broken line is described in text.



the case of $\tau = 0.5$, an appropriate value of D to match the shape of the opposition peak is ~ 0.004 . The multiple contributions needed to match the phase curves are $x_V = 0.10$ and $x_B = 0.0$ as shown in Figure 12. Since the largest opposition effect will be obtained when $x = 0.0$, it is not possible to produce the even larger opposition effect observed in the UV and R (cf. Figure 19) in the case of $\tau \leq 0.5$. The lower limit of τ will, therefore, be $\tau_{\min} > 0.5$.

To investigate the effects of choosing a larger optical thickness, we have also carried out computations for $\tau = 2$. In this case, we find $D \sim 0.013$ and multiple scattering contributions of $x_V = 0.40$ and $x_B = 0.28$ from Figure 13. The larger fractions of multiple scattering are necessary to dilute the larger shadowing effect produced by primary scattering as τ increases. The broken line in Figure 13 is drawn from the same reasoning discussed in the case $\tau = 0.7$. The appropriate theoretical brightness curve, therefore, will be quite similar to the broken line in Figure 13. The corresponding albedo range is estimated to be $0.7 \lesssim a_B \lesssim 0.8$ and $0.85 \lesssim a_V \lesssim 0.9$ from comparison of Figures 9 and 13. Summarized results for $\tau \neq 1$ are given in Table II.

In addition to the lower limit for the absolute surface brightness R_V^0 , we must investigate the effect on the model of choosing the apparent mean observational value $R_V^0 \sim 1.1$. The range of D and x which match the phase curves remains unchanged, since the phase curves measure only relative brightness. The particle albedos are increased, but the requirement that $a_R \leq 1$ in the red provides also an upper limit on a_V and a lower limit on D (through interaction with x).

Figure 12: Theoretical phase curves for $\tau = 0.5$ which match the observations. Same notation as Figure 7. Compare with Figures 7 and 10.

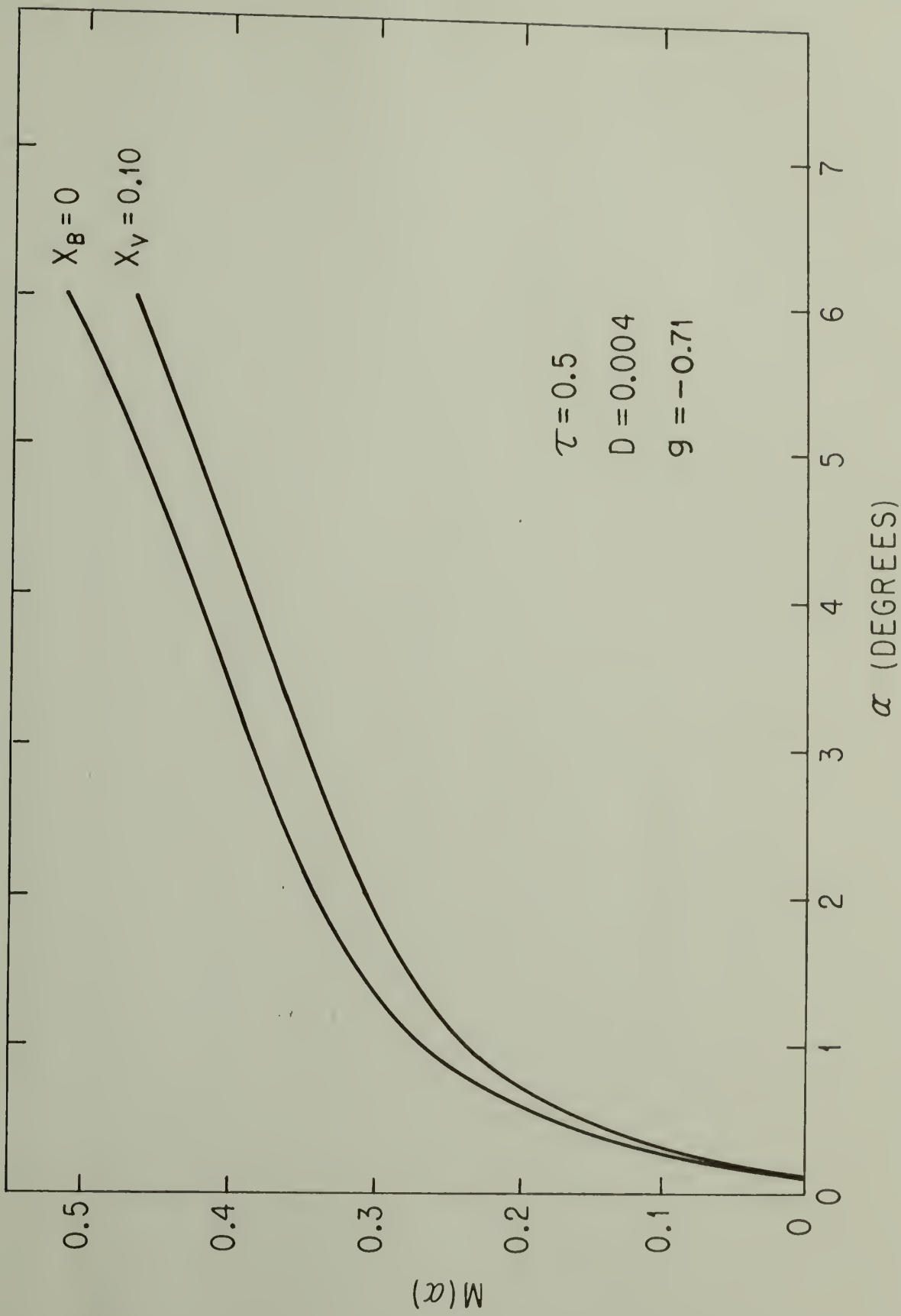


Figure 13: Theoretical phase curves for $\tau = 2.0$ which match the observations. Same notation as Figure 7. Compare with Figures 7, 10 and 12.

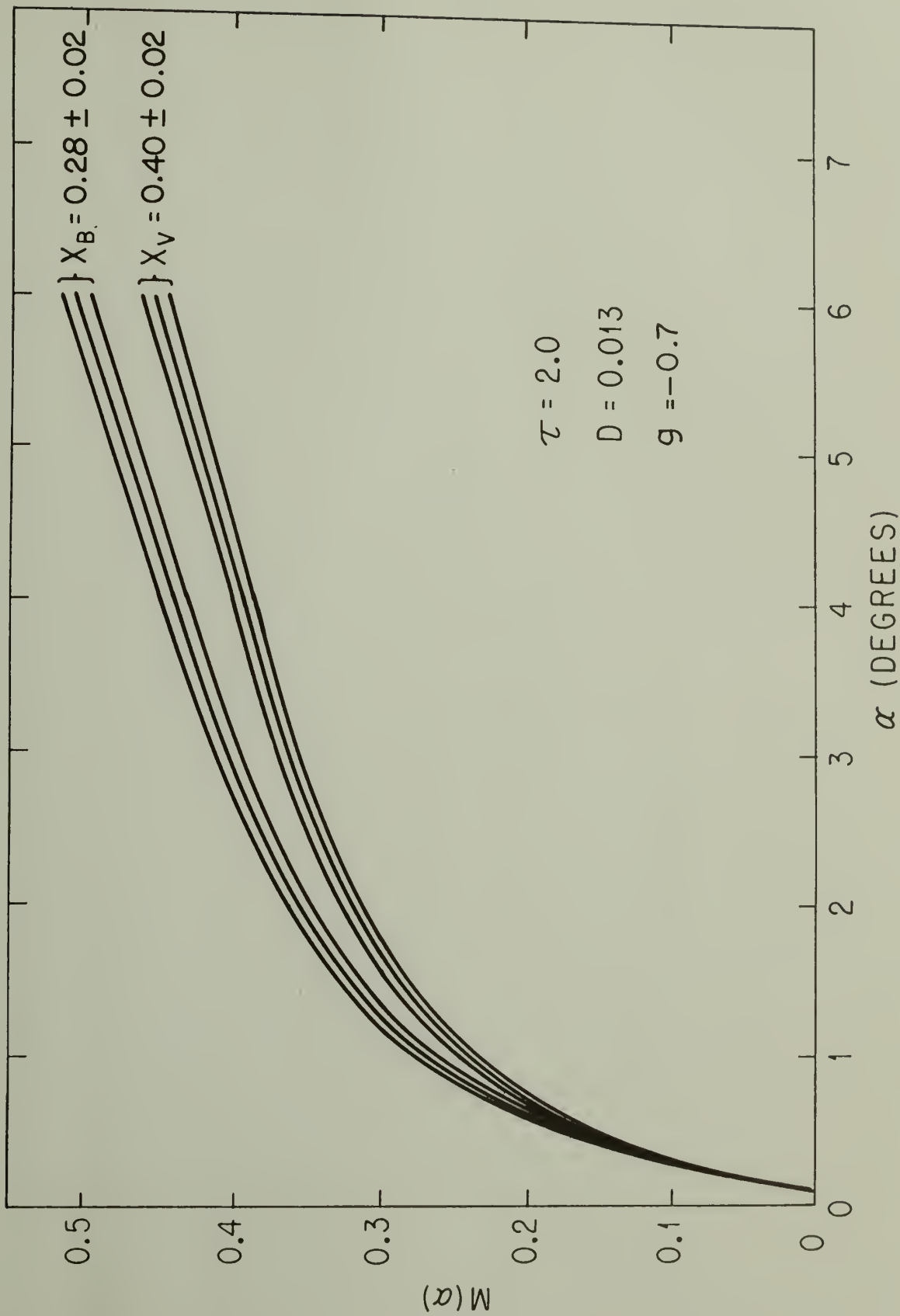


Figure 14: Diagram for comparison of observation and theory for
 $\tau = 2.0$ and $R_V^O = 1.0$. Same notation as Figure 11.

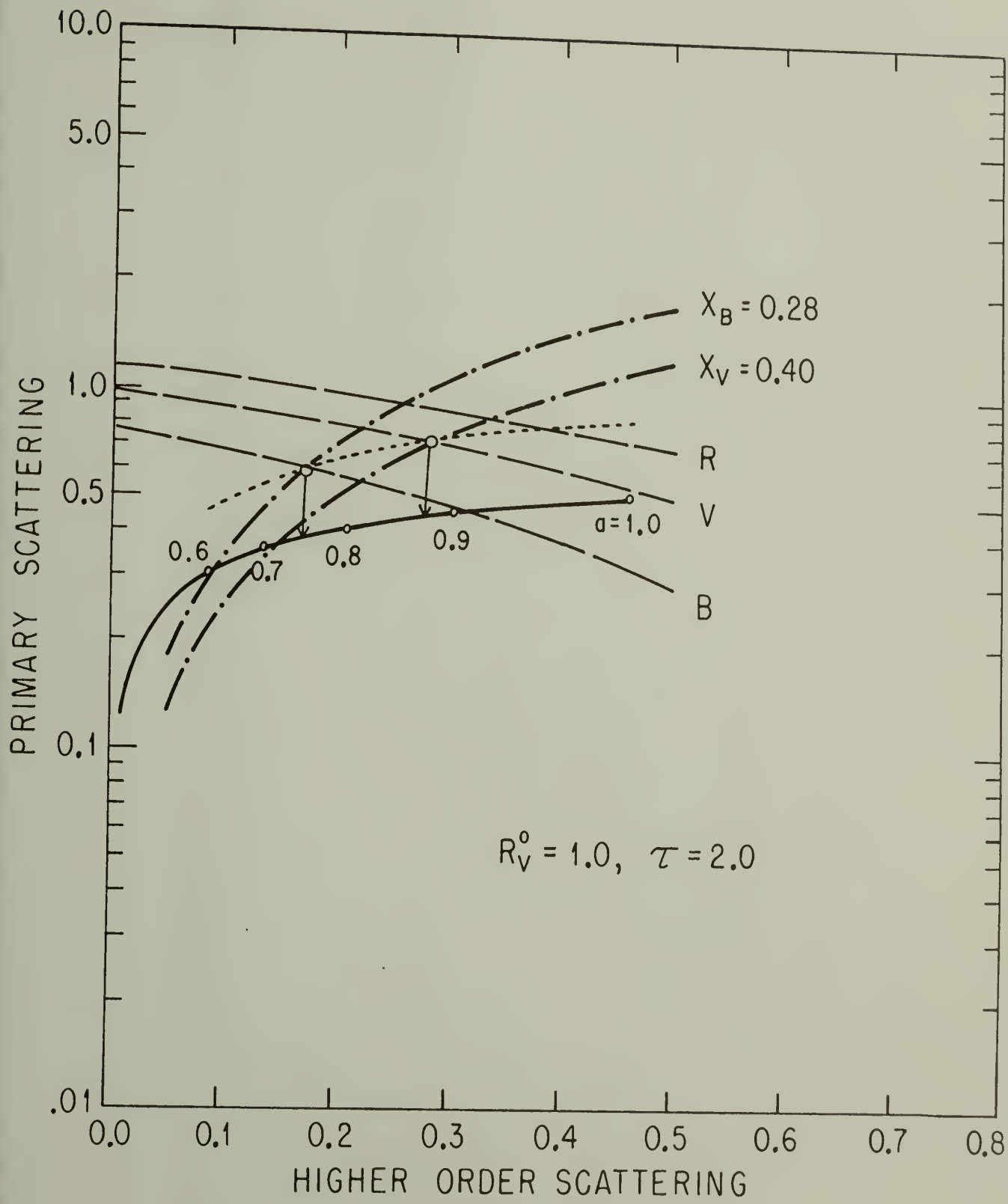


Table II: Summarized results are shown for ring optical depth
 $\tau \neq 1$.

TABLE II

Summarized Results for $\tau \neq 1$

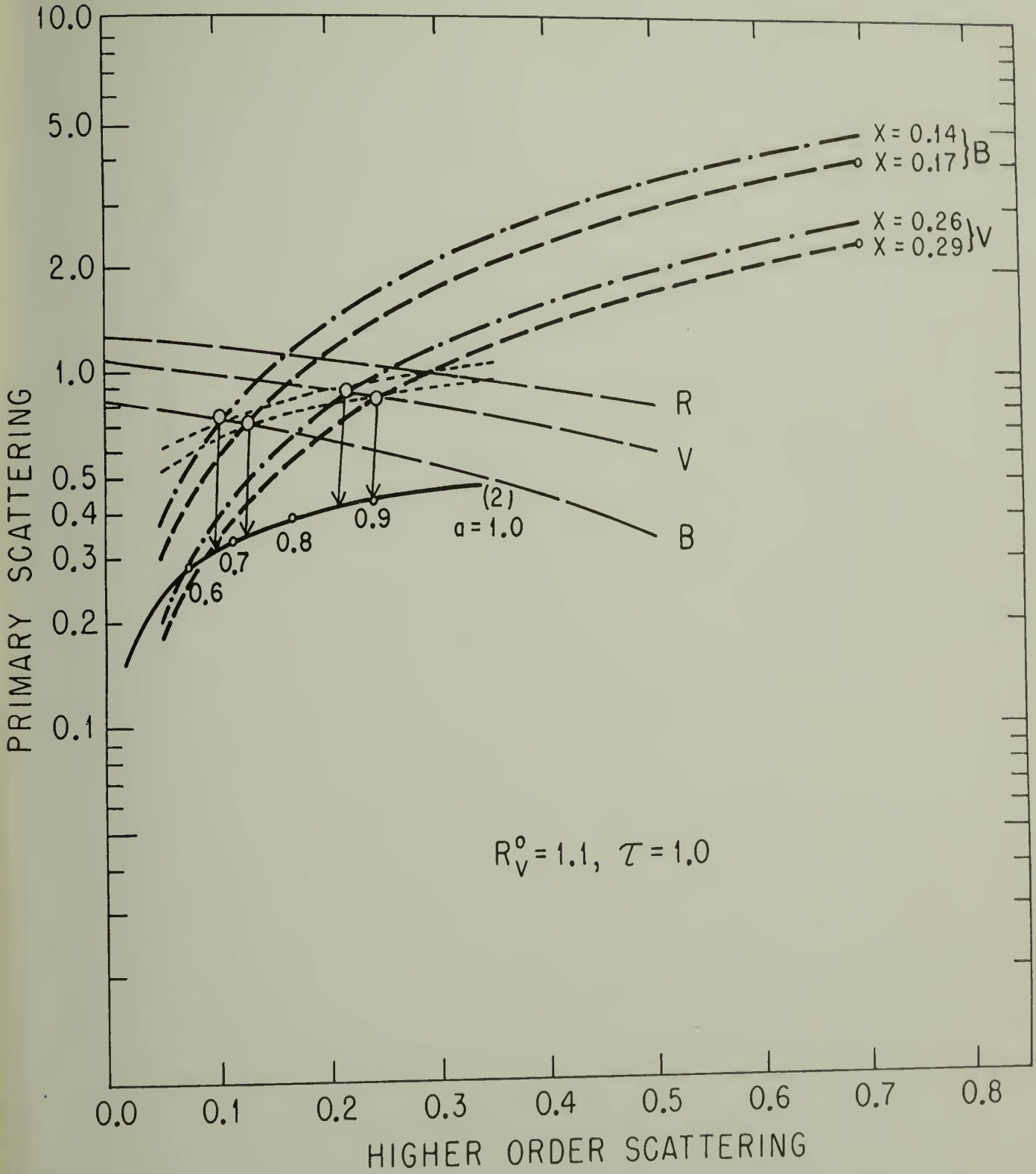
1. The lower limit of the optical depth is $\tau_{\min} > 0.5$
2. The albedos in V are rather insensitive to τ
3. The larger the optical thickness, the less backward scattering the phase function
4. The smaller the optical thickness, the smaller the volume density

Allowable Range of Parameters

Monodisperse Cases for $\tau = 0.7$ and $\tau = 2.0$

$\tau = 0.7$	$\tau = 2.0$
$0.005 \lesssim D \lesssim 0.007$	$0.011 \lesssim D \lesssim 0.014$
$0.6 \lesssim a_B \lesssim 0.7$	$0.7 \lesssim a_B \lesssim 0.8$
$0.85 \lesssim a_V \lesssim 0.9$	$0.85 \lesssim a_V \lesssim 0.9$

Figure 15: Diagram for comparison of observation and theory for $\tau = 1.0$ and $R_V^O = 1.1$. The solid line (2) is the theoretical brightness curve for an isotropic phase function. The broken lines are described in text. Other notation is the same as Figure 6. This shows the allowable range of albedos for $\tau = 1$ and $R_V^O = 1.1$.



As a result, the allowable range of particles albedo is reduced relative to that for a lower absolute surface brightness. We find $0.85 \leq a_V \leq 0.90$, $0.66 \leq a_B \leq 0.72$, and $0.01 \leq D \leq 0.012$ for $\tau = 1$ from Figure 15. The broken lines in Figure 15 are obtained from the same procedure as described in drawing the broken lines b, and c in Figure 9. The corresponding phase function has approximately a 10% larger backward peak than in the previous case, so that the phase integral becomes $q \sim 1.95$ instead of 2.1.

A. Distribution of Particle Sizes. Up to this point we have assumed that the ring particles can be characterized by a single effective radius ρ . Within the framework of this assumption we can determine that size if we know the geometric thickness of the rings t . From the definitions of the optical depth $\tau = \pi \rho^2 n t$ and the fractional volume $D = (4/3)\pi \rho^3 n$ we find that

$$\rho = \frac{3}{4} \frac{D}{\tau} t . \quad (32)$$

The ring thickness has been measured by Kiladze (1969) and Focas and Dollfus (1969) to be approximately 2 kilometers. Taking $\tau = 1$, $D = 0.01$ and $t = 2$ kilometers, we find that $\rho = 15$ meters. This size is consistent with the recent radar results obtained by Goldstein and Morris (1973).

The above result is quite deceptive, however. To see this we must investigate the possible influence on our results of allowing for a distribution in particle sizes. Let us assume that the number of particles with radii between ρ and $\rho + d\rho$ is given by

$$dn = f(\rho) d\rho$$

per unit volume. If we assume that the volume density D remains small enough so that the small element of area ε on a test particle in Figure 2 shielded from the sun and earth by a particle in the range $\rho \rightarrow \rho + d\rho$ is independent of the probability that it is shielded by a particle of any other radius, we may rewrite equation (6) for the first order reflected intensity including the shadowing effect and obtain

$$R_1^s = \left(\frac{a \Phi}{4\mu \mu_0} \right) \left(\pi \int_{\rho_1}^{\rho_2} f(\rho) \rho^2 d\rho \right) \times \quad (33)$$

$$\int_0^t \exp\left[-h' \left(\frac{1}{\mu} + \frac{1}{\mu_0} \right) \left(\pi \int_{\rho_1}^{\rho_2} f(\rho) \rho^2 d\rho \right) + \int_{\rho_1}^{\rho_2} f(\rho) C(\rho, h') d\rho \right] dh'$$

where the upper and lower limits on particle size have been labeled ρ_2 and ρ_1 . The rest of the theory remains the same.

The choice of possible forms for the particle distribution function is of course infinite. Bobrov has investigated the relation

$$f(\rho) = K\rho^{-s} \quad (34)$$

where K is a constant and s is a parameter describing the shape of the distribution. This distribution law is common in meteor astronomy, and of course can lead to a predominant number of quite small particles.

We have investigated the effect of a uniformly used particle distribution ($s = 0$) and also the cases $s = 2$ and 3 . We take

$\rho_1 = 0.2$ cm as the lower limit of the size distribution (cf. Bobrov, 1970). Diffraction does not shorten significantly the shadow of a particle when the radius of a particle is larger than 0.2 cm. If the radius of a particle is less than 0.2 cm, its shadow tends to decrease due to diffraction. Such small particles will not contribute to the shadowing effect which is the physical basis of the present ring model.

For $s = 0$ the results are quite similar to the monodisperse case. If we fix the optical thickness $\tau = 1.0$ and the geometric thickness $t = 2$ km, the value of D depends primarily on the upper limit ρ_2 of the size distribution. To obtain the necessary range of D ($0.008 \leq D \leq 0.012$), we must have $16 \text{ m} \leq \rho_2 \leq 24 \text{ m}$. The mean particle size is then $\langle \rho \rangle \sim 10 \text{ m}$. The parameters D and $\langle \rho \rangle$ are essentially independent of ρ_1 if $\rho_1 \leq 1 \text{ m}$.

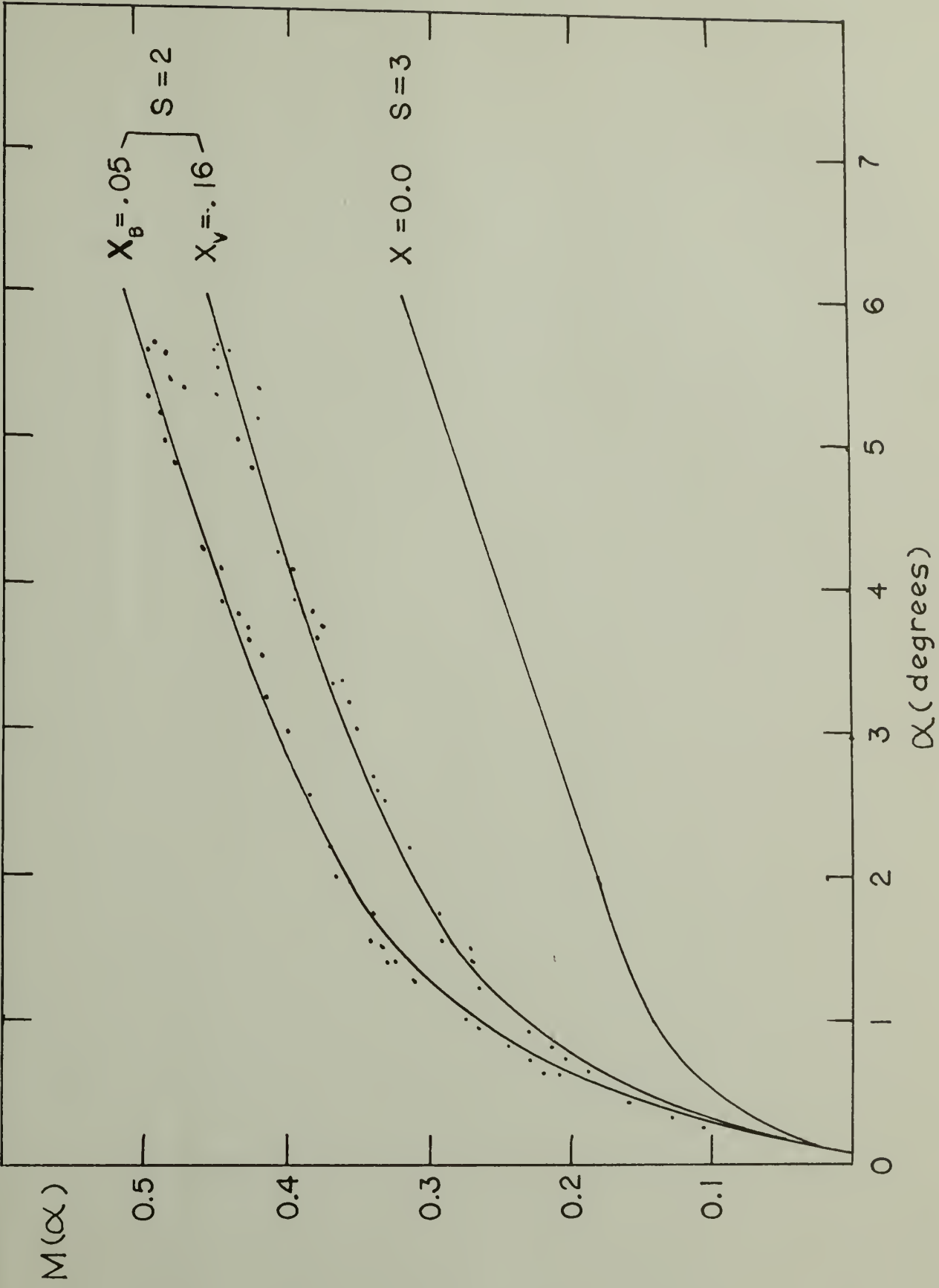
The corresponding upper limit of the particle size distribution when $s = 2$ is $20 \text{ m} \leq \rho_2 \leq 40 \text{ m}$. The range of permissible values for the volume density D is slightly increased ($0.007 \leq D \leq 0.013$). The corresponding range of permissible values for the multiple scattering contribution x is also increased, so that $0.16 \leq x_V \leq 0.23$ and $0.05 \leq x_B \leq 0.11$. The case of $\rho_2 = 40 \text{ m}$ and $\rho_1 = 0.2 \text{ cm}$ is shown in Figure 16. Although the mean particle size in this case is $\langle \rho^2 \rangle^{1/2} = 2 \text{ cm}$, we find that the results are quite insensitive to the lower limit ρ_1 of the particle size distribution provided that $\rho_1 \leq 50 \text{ cm}$ but do remain quite dependent upon the value of D . This shows that the shadowing effect in the case $s = 2$ continues to determine the volume density D quite precisely, but that the mean particle size

remains uncertain provided that it is large enough to produce the required geometric optics shadowing. But we can set the upper limit of the mean particle size from the corresponding limits $\rho_2 = 40 \text{ m}$ and $\rho_1 \leq 50 \text{ cm}$. We obtain the values of the mean particle size $\langle \rho \rangle \lesssim 2.2 \text{ m}$, $\langle \rho^2 \rangle^{1/2} \lesssim 4.5 \text{ m}$ and $\langle \rho^3 \rangle^{1/3} \lesssim 7.4 \text{ m}$. The most important one among them is probably $\langle \rho^2 \rangle^{1/2} \lesssim 4.5 \text{ m}$, because the geometric cross section of a particle is proportional to square of a particle radius.

We apply essentially the same method to estimate the albedo and the phase function in the case $s = 2$ as in the monodisperse case, except introducing a wavelength dependence in the particle phase function. We will discuss this method in detail in Section VI in relation to the discussion of the infrared brightness temperature of the rings. According to the analysis given in that section, we obtain the lower limit of the particle albedos $a_B \sim 0.42$ and $a_V \sim 0.72$ for the case of $s = 2$, $x_B = 0.05$ and $x_V = 0.16$. A slightly more backward phase function for the blue than the phase function for the visible is required for this case. The corresponding lower limits of the phase integral for these phase functions are $q_B \sim 1.0$ and $q_V \sim 1.4$. If we use the same method for the case $s = 2$, $x_B = 0.11$, and $x_V = 0.23$ as described in Section VI, we obtain the upper limit of the particle albedos to be $a_B \sim 0.6$ and $a_V \sim 0.82$. The corresponding upper limits of the phase integral are $q_B \sim 1.4$ and $q_V \sim 1.9$. The allowable range for the particle albedos and the phase integrals are, therefore,

$$0.42 \lesssim a_B \lesssim 0.6, \quad 0.72 \lesssim a_V \lesssim 0.82, \quad 1.0 \lesssim q_B \lesssim 1.4, \quad \text{and} \quad 1.4 \lesssim q_V \lesssim 1.9,$$

Figure 16: Theoretical phase curves for $\tau = 1$ in the polydisperse cases of $s = 2$ and $s = 3$ (see equation (34)) points from the observations of Franklin and Cook (1965). For $s = 2$, we use $D = 0.013$ and $g = -0.62$. For $s = 3$, we use $D = 0.07$ and $g = -0.67$.

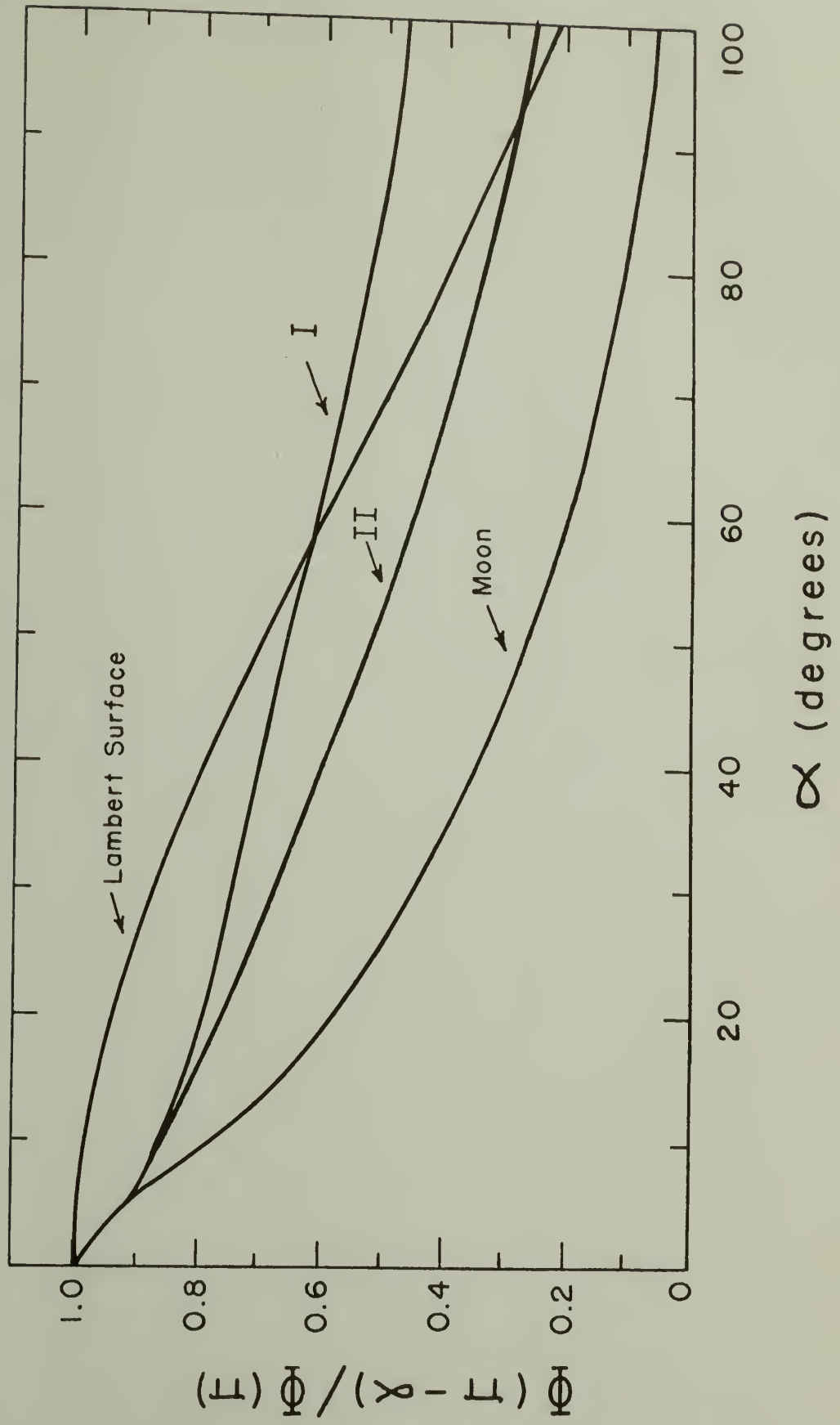


when $s = 2$.

On the other hand, the size distribution cannot be too sharply varying. When the parameter $s = 3$ in equation (34), it is not possible to obtain agreement with observations. As is seen from Figure 16, the opposition effect is too small when we take a wide range of particle size ($\rho_2 = 100 \text{ m}$ and $\rho_1 = 1 \text{ cm}$). The reason why the curve $x = 0$ for the case $s = 3$ is presented in Figure 16 is that we have a maximum opposition effect in the case $x = 0$ (no multiple scattering contribution) and the increasing of the value of x makes the situation worse. If $\rho_1 < 1 \text{ cm}$, then the opposition effect tends to be still smaller. The only way to make the opposition effect comparable to the observed data is to increase the value of ρ_1 up to the order of a meter. By narrowing the particle size range, we will have essentially the same situation as the monodisperse case, since the number of particles whose size $\sim \rho_1$ is dominant in the case of $s = 3$.

The shape of the particle phase functions are compared to those for the Moon and for a Lambert sphere in Figure 17. A Lambert sphere is a sphere whose surface at energy point has the characteristics of a Lambert surface as described before in Section IV. The curve I in Figure 17 is the phase function (4) given in Section IV and this phase function gives the best fit for Ring B in the monodisperse case. The curve II in Figure 17 is the phase function with the parameters $b = 0.991$, $g_1 = -0.26$, and $g_2 = -0.82$, which gives the particle albedo close to the lowest visual albedo in the case of $s = 2$. The phase integral for this is given by $q_V \sim 1.4$. The shape of these phase

Figure 17: Ring particle phase curves $\Phi(\pi - \alpha)/\Phi(\pi)$ for both the monodisperse case (curve I) and the polydisperse case of $s = 2$ (curve II) compared with lunar phase curve from Rougier (1934) and with phase curve for Lambert sphere.



functions is quite similar to the Moon near $\alpha = 0^\circ$, but the ring particle brightness (based on either the curve I or the curve II) falls off less rapidly with increasing α than does that of the Moon. This is in agreement with the results of Veverka (1973) for snow covered objects.

We may compare the results for the monodisperse and the polydisperse cases in Table III.

B. Tilt effect. We may test the validity of the type of model chosen here by comparison with other types of observations. Particularly important are the data on the surface brightness as a function of solar illumination angle θ_0 (tilt angle). Observations over a limited range of θ_0 have been made by Camichel (1958) and Focas and Dollfus (1969). More accurate and homogeneous measurements have been published by Price (1973), although this data includes both rings together. At $\theta_0 = 64^\circ$, the mean surface brightness of ring B is 20% greater than the mean of ring A and ring B (Franklin and Cook, 1965; Camichel, 1958). As a first approximation towards removing the effect of ring A from Price data, we may assume that this ratio applies also at other θ_0 . Price's data so corrected are plotted in Figure 18, together with Camichel's results scaled to agree with Price at $\theta_0 = 64^\circ$. The corresponding theoretical curves were computed for the cases (A) and (B), as follows. Case (A); $a_V = 0.9$ and the phase function (22) with $b = 0.995$, $g_1 = -0.16$, and $g_2 = -0.85$. This form of Φ gives the highest visual albedo in the monodisperse case and fits the observed phase curves and the mean absolute surface brightness $R_V^0 = 1.1$.

Case (B); $a_V = 0.75$, and the phase function with $b = 0.991$, $g_1 = -0.26$, and $g_2 = -0.82$. This form of Φ gives a particle albedo close to the lower limit in the cases we have investigated (cf. Table III).

The agreement between theory and observation is quite good for the case (A). For the case (B) the results are within the error range. These results clearly illustrate the importance of multiple scattering in the rings, since the surface brightness for primary scattering alone would decrease with increasing θ_o , in opposition to the multiple scattering model. Note that the reflection angle as viewed from the earth θ (see Figure 2) is approximately equal to θ_o , because of the plane nature of the solar system, except when $\theta_o \approx 0$.

Table III: Comparison between monodisperse particle size case and polydisperse cases is given.

TABLE III

Summarized results for $\tau = 1$ and $t = 2$ km

1. monodisperse case

mean particle size ~ 15 m

$D \sim 0.01$

$0.65 \leq a_B \leq 0.75$ and $0.82 \leq a_V \leq 0.9$

$q_B = q_V \sim 2.0$

$0.31 \lesssim p_B \lesssim 0.36$ and $0.4 \lesssim p_V \lesssim 0.43$

2. polydisperse cases (see equation (34))

a. $s = 0$ (uniform distribution)

the results are quite similar to the monodisperse case

b. $s = 2$

mean particle size $\lesssim 4.5$ m

$D \sim 0.01$

$0.42 \leq a_B \leq 0.6$ and $0.72 \leq a_V \leq 0.82$

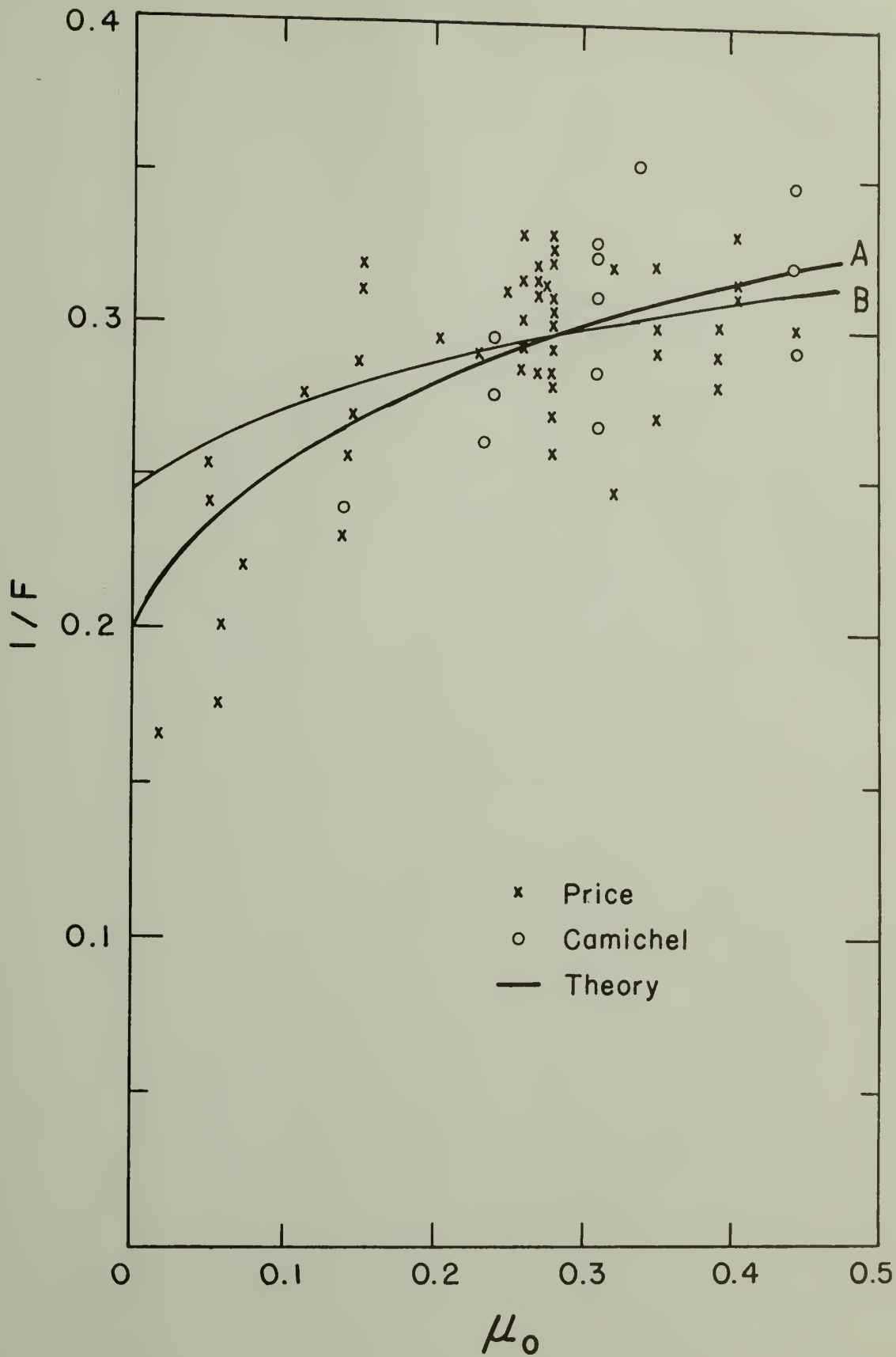
$1.0 \leq q_B \leq 1.4$ and $1.4 \leq q_V \leq 1.9$

$0.42 \leq p_B \leq 0.43$ and $0.43 \leq p_V \leq 0.51$

c. $s = 3$

no agreement with the data

Figure 18: Surface brightness $I/F = \mu_0 R(\alpha = 6^\circ)$ for ring B versus $\mu_0 = \cos \theta_0$ where θ_0 is the solar illumination for the angle V wavelength band. Observational points from Price (1973) and Camichel (1958), corrected as described in text. Theoretical curves computed from equation (11) for two choices of parameters (see text).



SECTION VI

INFRARED BRIGHTNESS TEMPERATURE

Since the infrared (IR) brightness temperature, T_{IR} , is related to the albedo a in the visible and since also the observational data indicate that there exists a change in the IR brightness temperature with tilt angle (Murphy, 1973; Allen and Murdock, 1971; Low, 1966), it is important to see if the IR results are compatible with our basic model. In order to calculate the IR brightness temperature of the rings, we have to consider three different heating sources: the solar flux, the flux from Saturn's ball and the heating due to neighboring particles within the ring layer.

A. Procedure. The basic procedure in treating this problem is the following. We need first to solve the multiple scattering problem at visual wavelengths as a function of tilt angle. If we know the particle albedos at given wavelengths, we can then calculate the total solar energy absorbed by the rings and consequently the IR brightness temperature of the rings due to the solar heating of the particles. But each particle is also heated by thermal radiation from neighboring particles. Using the above results and the condition of radiative equilibrium, we can iterate the IR brightness temperature distribution to include this mutual heating among the ring particles. Finally the effect of Saturn's ball can be included.

The condition of radiative equilibrium is expressed by equation (35) which relates the mean intensity of radiation J to the source function S .

$$4\pi \int d\lambda K_\lambda J_\lambda = \int d\lambda \int_{4\pi} d\Omega K_\lambda S_\lambda \quad (35)$$

$$J_\lambda = \frac{1}{4\pi} \int_{4\pi} d\Omega I_\lambda \quad (36)$$

$$S_\lambda = \frac{a_\lambda}{4\pi} \int_{4\pi} d\Omega I_\lambda + (1 - a_\lambda) B_\lambda(T) \quad (37)$$

$$B_\lambda(T) = \frac{2hc^2}{\lambda^5} \frac{1}{e^{hc/kT} - 1} \quad (38)$$

where the integrations are over the sphere (see the definition of coordinates in Figure 2),

K_λ = total extinction coefficient (absorption plus scattering)

h = Planck's constant (= 6.63×10^{-27} erg sec)

c = velocity of light (= 3×10^{10} cm/sec)

k = Boltzman's constant (= 1.38×10^{-16} erg/deg)

T = temperature

and we have indicated explicitly the dependence on wavelength λ of the intensity I_λ and the albedo a_λ . Equation (35) expresses the physical requirement that in radiative equilibrium all the radiant energy which interacts with the ring particles (left side of the equation) must be either scattered or re-emitted thermally (right side of the equation). Since scattering returns as much energy to the beam as it removes (e.g., Mihalas 1970) and since at expected ring temperatures the thermal emission is confined to the IR, equation (35) can be

rewritten as

$$4\pi \left[\int_{\text{op}} d\lambda \kappa_{\text{op}} J_{\text{op}} + \int_{\text{IR}} d\lambda \kappa_{\text{IR}} J_{\text{IR}} \right] = \int_{\text{IR}} d\lambda \int_{4\pi} d\Omega \kappa_{\text{IR}} (1-a_{\text{IR}}) B_{\text{IR}}(T) \quad (39)$$

where κ is the absorption coefficient and the notations "OP" and "IR" refer to the optical portion of the spectrum ($0.3\mu - 1.1\mu$) and the infrared portion of the spectrum, respectively. Since our model assumes large particles in the rings to produce shadowing and thus geometric optics ($K_\lambda = \text{const}$), we may divide both sides of equation (39) by K_λ and obtain

$$4\pi \left[\int_{\text{op}} d\lambda (1-a_{\text{op}}) J_{\text{op}} + \int_{\text{IR}} d\lambda (1-a_{\text{IR}}) J_{\text{IR}} \right] = \int_{\text{IR}} d\lambda \int_{4\pi} d\Omega (1-a_{\text{IR}})^2 B_{\text{IR}}(T) \quad (40)$$

where we recall that the albedo a is the ratio of the scattering to the total extinction so that $\kappa/K = 1 - a$.

We define $E^\ominus(\zeta, \mu_\ominus) \cdot K_\lambda$ as the amount of solar energy absorbed by the rings per unit area, unit time, and unit optical depth at the solar illumination angle $\theta_\ominus = \arccos \mu_\ominus$ and optical depth ζ . We can, therefore, set the left side of equation (40) equal to $E^\ominus(\zeta, \mu_\ominus)$ if we ignore thermal radiation by the rings and Saturn's ball. We assume $a_{\text{IR}} = 0$ for simplicity (i.e., unit emissivity). After taking into account the difference (by $E_\lambda \mu_\ominus / \pi$) between the absolute solar flux and our flux definition and using equations (10) and (34), the left side of equation (40) becomes

$$\begin{aligned}
E^\ominus(\zeta, \mu_0) = & \left[\int_{0.3\mu}^{1.1\mu} E_\lambda (1 - a_\lambda) d\lambda + \int_{1.1\mu}^{4.0\mu} E_\lambda d\lambda \right] e^{-\zeta/\mu_0} \\
& + 2\mu_0 \int_{0.3\mu}^{4.0\mu} d\lambda E_\lambda (1 - a_\lambda) \left[\int_{-1}^1 \sum_{n=1}^{\infty} (a_\lambda)^n I_n d\mu \right]
\end{aligned} \tag{41}$$

where the solar energy flux E_λ is given by Allen (1955) and I_n is the n th order scattered intensity obtained from equation (12). Since the solar flux E_λ for either $\lambda < 0.3\mu$ or $\lambda > 4.0\mu$ is negligibly small, we integrate over the finite wavelength range ($0.3\mu \leq \lambda \leq 4.0\mu$).

Initially we ignore the mutual heating among the ring particles. Since the right side of equation (40) is just $\sim T^4$, the IR temperature distribution due to the absorbed solar flux is found from equation (42):

$$T^{(1)}(\zeta, \mu_0) = \sqrt[4]{E^\ominus(\zeta, \mu_0)/4\sigma} \tag{42}$$

where $\sigma = 5.67 \times 10^{-5} \text{ erg.s.cm}^{-2}.\text{sec}^{-1}.\text{deg}^{-4}$ (Stefan - Boltzman constant). The resulting temperature distribution is shown by the curve T^\ominus in Figure 24 below.

We may then include the effects of mutual heating among the ring particles. Using the formal solution of the transfer equation (43)

$$\begin{aligned}
I(\zeta, \mu) = & \int_{\zeta}^{\tau} S(t) e^{-(t - \zeta)/\mu} \frac{dt}{\mu} & (0 \leq \mu \leq 1) \\
I(\zeta, \mu) = & - \int_0^{\zeta} S(t) e^{(\zeta - t)/\mu} \frac{dt}{\mu} & (-1 \leq \mu \leq 0)
\end{aligned} \tag{43}$$

and equation (37) with $T^{(1)}$ given by equation (42), we can rewrite equation (36) as

$$J_{\text{IR}}^{(1)}(\zeta, \mu_0) = \frac{1}{2} \left[\int_0^\zeta B(T^{(1)}(t, \mu_0)) E_1(\zeta - t) dt + \int_\zeta^\tau B(T^{(1)}(t, \mu_0)) E_1(t - \zeta) dt \right] \quad (44)$$

where $E_1(X)$ is the first order exponential integral and is given by

$$E_1(X) = \int_1^\infty \frac{e^{-Xz}}{z} dz \quad (45)$$

Equation (44) is known as Milne's equation. To compute $J_{\text{IR}}^{(1)}$ we use the numerical method given by Mihalas (1967). The condition of radiative equilibrium (equation (40)) becomes

$$E^{\ominus}(\zeta, \mu_0) + 4\pi \int_{\text{IR}} J_{\text{IR}}^{(1)}(\zeta, \mu_0) d\lambda = 4\sigma(T^{(2)}(\zeta, \mu))^4 \quad (46)$$

By solving equation (46), we can find a new IR temperature distribution $T^{(2)}(\zeta, \mu_0)$. Substituting $T^{(2)}$ into equation (44) in place of $T^{(1)}$, we get $J_{\text{IR}}^{(2)}$ and then $T^{(3)}$ is found from equation (46), and so on. About 6 iterations are enough to give the final temperature distribution $T^{(f)}$ for a given value of μ_0 . We have assumed isotropic scattering in the IR. There exists a possibility of anisotropic scattering or emission from only one side of a particle, but we will discuss this point later.

B. Albedo spectrum. In order to actually compute $T^{(f)}$, we must now estimate the particle albedo at different wavelengths. We have found that for the particle size distribution given by equation

(34), we can obtain the lower limit of the albedo in the optical range when $s = 2$. We will investigate this $s = 2$ case. Since there are many uncertainties in determining the albedo in the red (cf. Section IV), we will consider two extreme cases.

Case A: This is the case which ignores the observed opposition effect in the red (Irvine and Lane, see Figure 19) and thus gives high values for the albedo in the red and near infrared. (For a given measured brightness at $\alpha \approx 0$, the greater the opposition effect, the smaller the particle albedo.) We can estimate the albedos throughout the optical range from the results in the previous section for a_B and a_V and by scaling the reflectivity measurements of Lebofsky et al. (1970). Since only relative spectra for $\lambda > 1.1\mu$ are now available, it is very difficult to estimate the albedo for these wavelengths. We should stress the desirability of reflectivity observations on an absolute scale beyond 1 micron. We shall assume that in the IR range beyond 1 micron the albedo may be obtained by using Debye's asymptotic form of the Mie equations for a particle whose size is much larger than the wavelength (Irvine, 1965). If we use the refractive index data for ice particles at $\lambda \sim 1.1\mu$ (Irvine and Pollack, 1968), the resulting albedo in this range is found to be about 0.06. The albedo spectrum, obtained from the above method, is shown by the curve A in Figure 20.

Case B: Irvine and Lane's observations (1973) indicate that the amplitude of the opposition effect shows a maximum towards the ultraviolet (UV) and also towards the red (R) and shows a minimum in

Figure 19: Magnitude of the opposition effect for Saturn's rings.
Closed circles are narrow band results, open circles
are UBV data. Data from Irvine and Lane (1973).

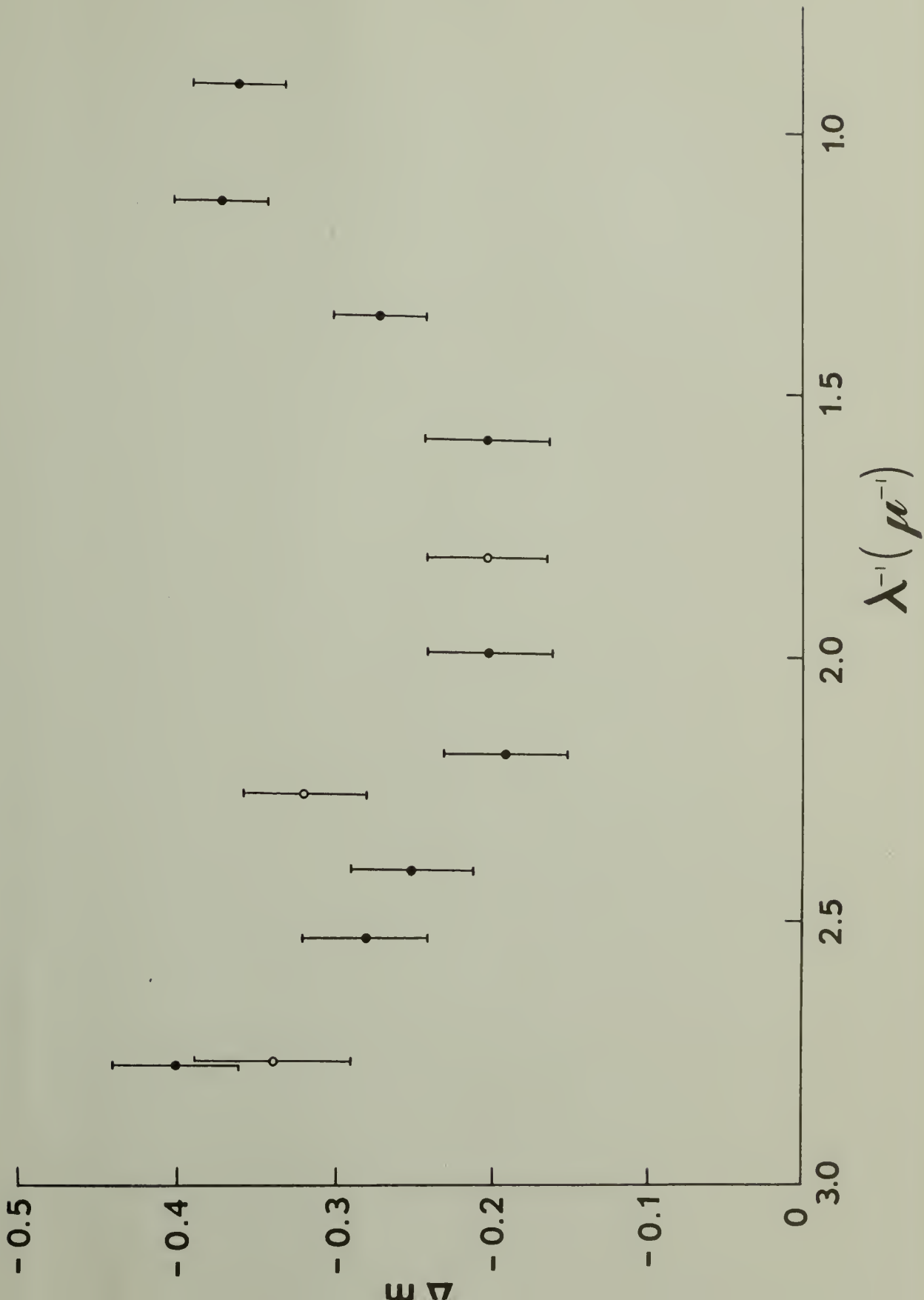
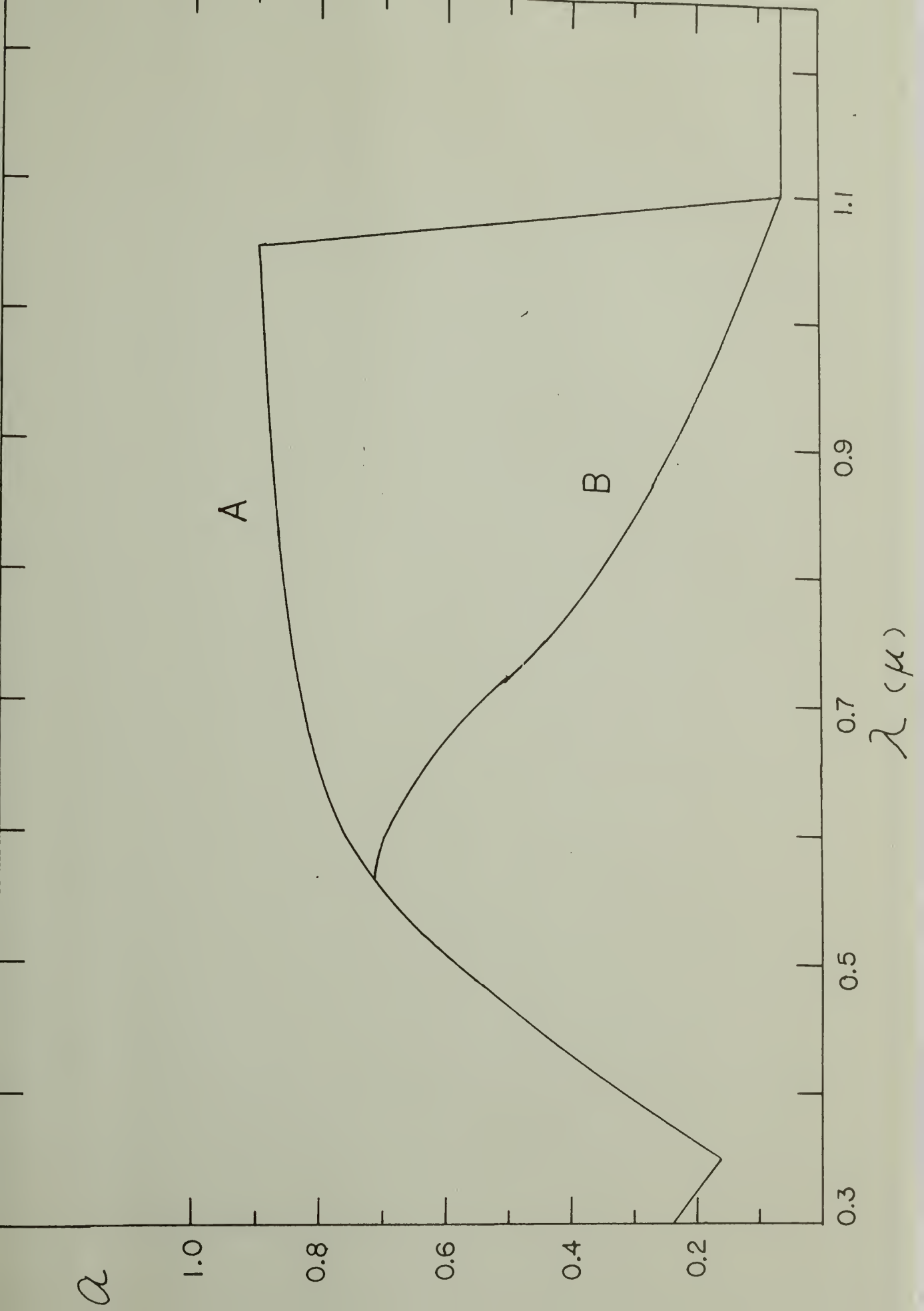


Figure 20: Ring particle albedo versus wavelength. The curve A and B are based on the case A and B, respectively. See text.



the V (Figure 19). We could lower the albedo in the red if we include such a large amount of opposition effect in the R.

Let us consider the case $s = 2$ in detail. The lower limit of multiple scattering contribution is found to be $x_B = 0.05$ and $x_V = 0.16$ in the Bands B and V, respectively (Figure 16). If we apply the same method in determining the albedo as described in section IV, the intersecting point P' between the curve $x = 0.05$ and the curve B in Figure 21 gives $a_B \sim 0.42$. The point P give $a_V \sim 0.72$. Although we need only one phase function for the blue and visual in the monodisperse case, we need a slightly more backward phase function for the blue than the phase function for the visible when $s = 2$. Since the appropriate theoretical absolute brightness curves for the B and V are similar to the theoretical brightness curves (3) and (2) shown in Figure 21, the corresponding phase functions for the B and V are similar to the curves (3) and (2) in Figure 22, respectively. We find that the phase integrals for the B and V are $q_B \sim 1.0$ and $q_V \sim 1.4$, respectively.

According to the reflectivity data of Irvine and Lane, the brightness intensity at $\lambda \sim 0.72\mu$ is stronger than in the visible by 1.4 if we include the opposition effect, which increases the brightness by $\sim 8\%$. Since the amount of the observed opposition effect at $\lambda \sim 0.72\mu$ is roughly the same as in the blue, the intersecting point Q (in Figure 21) between the curve $x = 0.05$ and the observed brightness curve $\lambda \sim 0.72\mu$ gives the albedo at $\lambda \sim 0.72\mu$ and this value is found to be 0.5 from Figure 21. The appropriate phase function at

Figure 21: Diagram for comparison of observation and theory. Same notation as Figure 6. Polydisperse case of $s = 2$ (see equation (34)), $\tau = 1$, $D = 0.013$. Theoretical brightness curves for four different phase functions (shown in Figure 22).

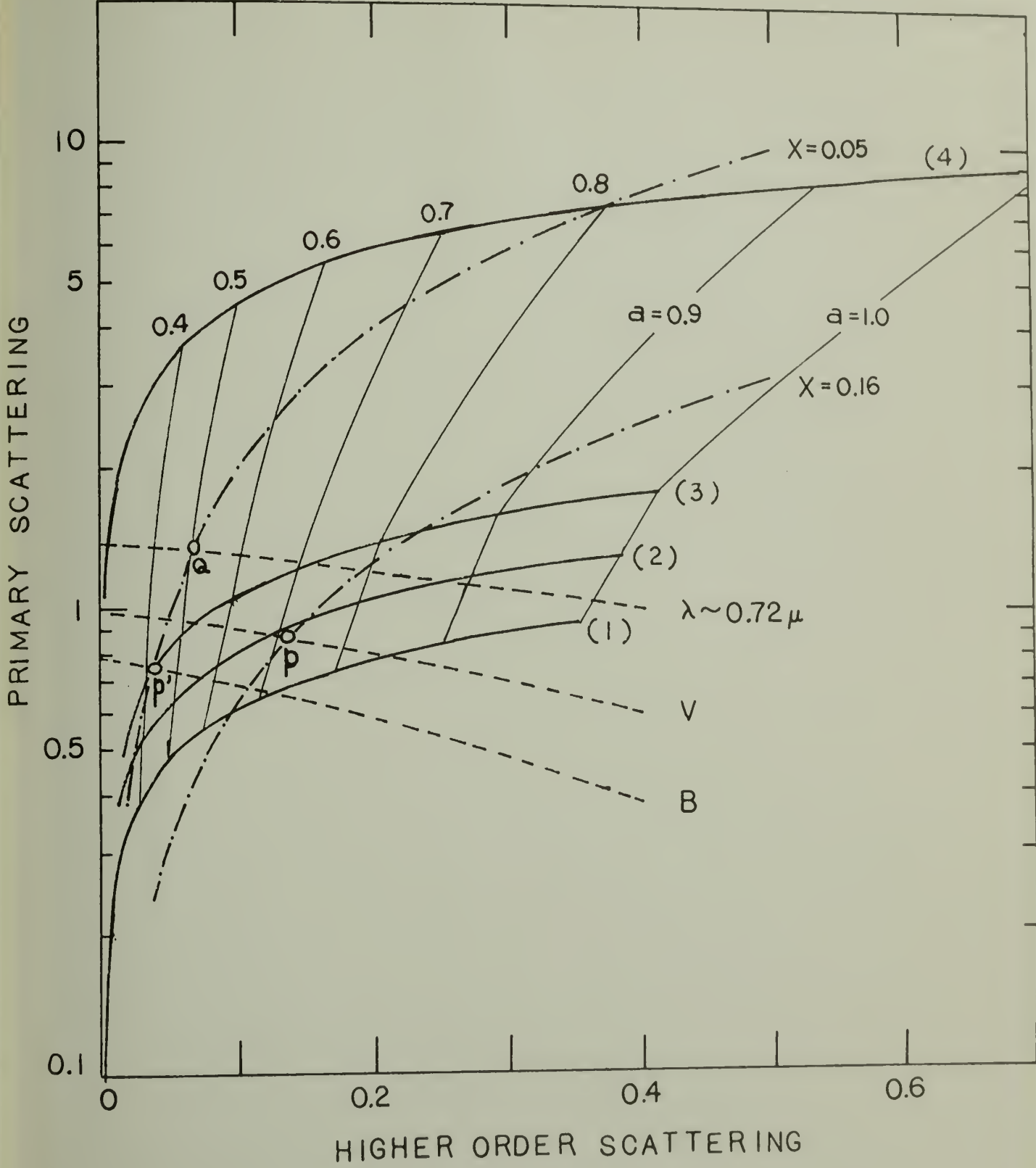


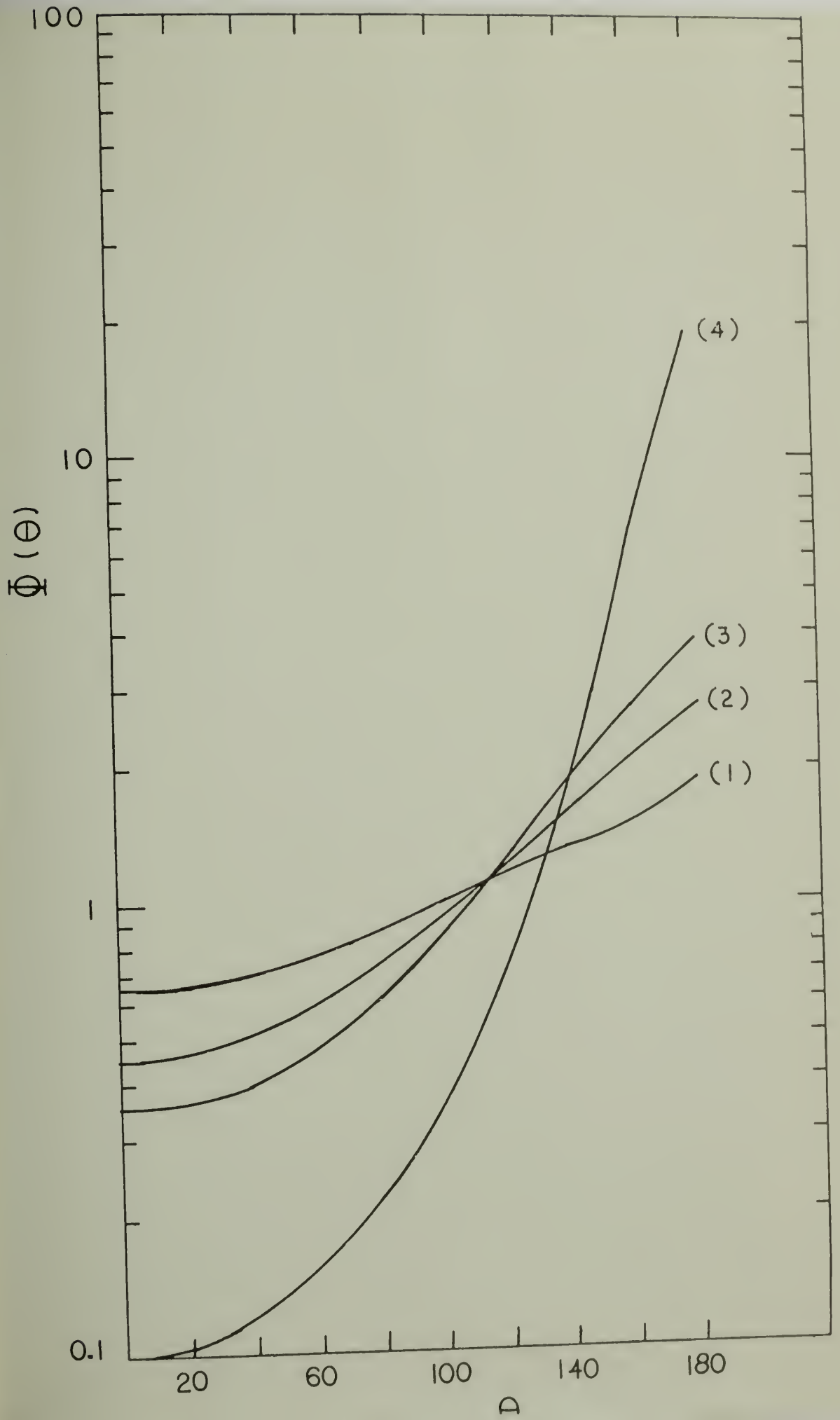
Figure 22: Four sample phase functions ϕ (see equation (22)) used for the calculations illustrated in Figure 21.

(1) $b = 0.995, g_1 = -0.14, g_2 = -0.84$

(2) $b = 0.991, g_1 = -0.26, g_2 = -0.82$

(3) $b = 0.985, g_1 = -0.35, g_2 = -0.81$

(4) $b = 0.0, g_1 = 0.0, g_2 = -0.7$



$\lambda \sim 0.72\mu$ is more backward scattering than the phase function (3). If we use the reflectivity data of Lebofsky et al. instead, the brightness intensity at $\lambda \sim 0.72\mu$ becomes 1.2 times that in the visible. This leads to an albedo at $\lambda \sim 0.72\mu$ of 0.47. In both cases we thus obtain an albedo at $\lambda \sim 0.72\mu$ of about 0.5 assuming that the shape of the phase curve at $\lambda \sim 0.72\mu$ is similar to that of the phase curve in the blue. When $\lambda \sim 1\mu$, x must be close to zero to satisfy the observed pronounced opposition effect. If $x \sim 0$, it is difficult to estimate the albedo from Figure 21. Since we know the albedo at $\lambda \sim 1.1\mu$ ($a_{IR} = 0.06$), we may obtain the albedo spectrum B (shown in Figure 20) by extrapolation. The appropriate phase function at $\lambda \sim 1.0\mu$ should be very strongly backward scattering, very similar to the phase function (4) in Figure 22, to satisfy the observed high reflectivity data.

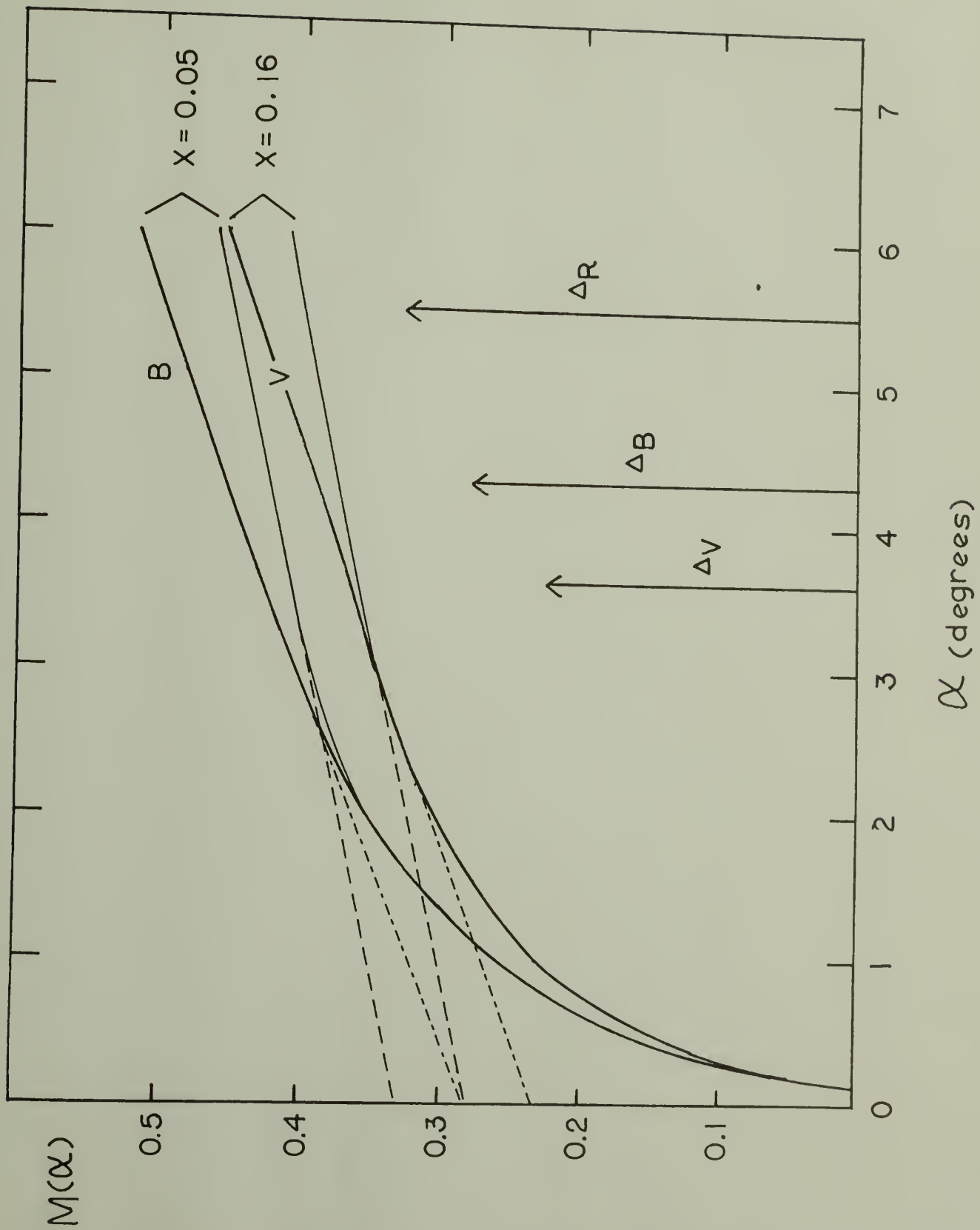
The important question is whether it is possible to have such a big change in the phase function towards longer wavelengths. The large particles which produce shadowing are expected to have phase functions nearly independent of wavelength. Let us consider that there exist lots of very fine particles which are not responsible for the shadowing mechanism but play a significant role in the scattering process. Deirmendjian (1962) computed the shape of phase function for a micron size particle at different wavelengths. These Deirmendjian-type phase functions have in general a strong forward diffraction peak and a small backward peak and both peaks tend to become less significant with increasing wavelength. It is, therefore, unlikely for such very

fine particles to increase backward scattering as the wavelength increases.

In summary, the albedo curve (B) in Figure 20 is one extreme case which fits the optical data, including a large opposition effect in the red, if we allow the phase function to change freely with λ . The albedo curve (A) is another kind of extreme case which does not include the observed opposition effect in the red, but otherwise fits the optical data. A possible answer to satisfy both opposition effect data and high reflectivity in the red is that the shape of the ring phase curve in the red might be different from that in the visual and the blue. For example, as is seen from Figure 23, we have the opposition effect of $0.28 \text{ mag/arcsec}^2$ with $x = 0.16$ if the slope of the phase curve is less steep than in the visual. Since the amount of the opposition effect ($0.28 \text{ mag/arcsec}^2$) in the blue is approximately equal to that at $\lambda \sim 0.72\mu$, the intersecting point between the dashed curve $\lambda \sim 0.72\mu$ and the dash dot curve $x = 0.16$ from Figure 21 gives an albedo of 0.8 at $\lambda \sim 0.72\mu$. The theoretical brightness curve in this case will be between the brightness curves (3) and (2). The corresponding particle phase function at $\lambda \sim 0.72\mu$ will be between the curves (3) and (2) in Figure 22.

At $\lambda \sim 1.0\mu$ the observed opposition effect is about $0.34 \text{ mag/arcsec}^2$. We have an opposition effect of this amount with $x = 0.05$ if the slope of the phase curve is less steep than in the blue. Since the observed absolute brightness at $\lambda \sim 1.0\mu$ is about equal to that in the visual, the intersecting point between the dashed curve V and

Figure 23: Diagram which shows the change in the magnitude of the opposition effect as the slope of the linearly increasing portion of the phase curve changes. Thick solid curves B and V are the theoretical phase curves which match the observations of Franklin and Cook (1965). Thin solid curves with flatter slope in the linearly increasing portion indicate the increase in the magnitude of the opposition effect. ΔV , ΔB and ΔR are the observed magnitude of the opposition effect in V, B and R as determined by Irvine and Lane (1973). Note that the shape of the phase curve in R, and hence the slope of the linearly increasing portion, has never been measured.



the dash dot curve $x = 0.05$ from Figure 21 gives an albedo at $\lambda \sim 1.0$ of 0.45. The corresponding phase function in this case will be slightly more backward scattering than the phase function (3) in Figure 22. These results are based on the observations of Irvine and Lane. When we use the reflectivity measurements of Lebofsky et al., we obtain in general the same results except for slight changes in the albedo and the phase function. The appropriate particle phase function for the red would, therefore, be very similar to that for either the blue or the visual except that it would be more slowly increasing near 180° . We do not need a strong backward phase function such as the phase function (4). The appropriate particle albedos for the red would be between the albedo spectrum curves A and B. Since the complete ring phase curve in the red is not available yet, we will not go further into this postulate, except to stress that the situation could be much clarified if a good observational phase curve for the rings were available at a wavelength $\lambda \gtrsim 0.7\mu$.

C. Results. In Figure 24, $T^{(1)}$ and $T^{(f)}$ are shown by the curves T^\ominus and $T^{\ominus+D}$, respectively. These results are based on the albedo curve (A). The curve $T^{\ominus+D+h}$ in Figure 24 is the IR brightness temperature distribution including the three different heating sources, the Sun, Saturn's ball and the mutual heating within the ring layer. In calculating $T^{\ominus+D+h}$ we assume that Saturn's infrared radiation alone is sufficient to heat the rings isothermally to $\sim 50^\circ$ K (Cuzzi and Van Blerkom, 1974). We found that the mutual heating among the ring particles has more effect on the IR brightness temperature of the rings

than the infrared radiation from Saturn's ball. The results of the IR brightness temperature distribution based on the albedo curve B are shown in Figure 25.

Since the measured brightness temperature T^* is obtained by equating the observed emergent flux from the rings and the theoretical flux from an isothermal black body, the rings brightness temperature T^* is calculated from equation (47):

$$B_{\lambda}(T^*)(1 - e^{-\tau/\mu_0}) = \frac{1}{\mu_0} \int_0^{\tau} e^{-\zeta/\mu_0} B_{\lambda}(T^{\theta+D+h}(\zeta, \mu_0)) d\zeta \quad (47)$$

where we continue to assume unit emissivity for the ring particles in the IR. Low (1965, 1966) measured the infrared brightness temperature of the ring B and set an upper limit to the brightness temperature of $T^* \sim 80^{\circ}\text{K}$ at 10μ when $\theta \sim 81^{\circ}$ and $T^* < 60^{\circ}\text{K}$ at 20μ when $\theta > 85^{\circ}$. Allen and Murdock (1971) found $T^* \sim 83 \pm 3^{\circ}\text{K}$ at $\lambda \sim 12\mu$ when $\theta \sim 73^{\circ}$. More recent observations by Murphy et al. (1972) and Murphy (1973) found $T^* \sim 90^{\circ} \pm 3^{\circ}\text{K}$ and $T^* \sim 94 \pm 2^{\circ}\text{K}$ at $\lambda \sim 20\mu$ when $\theta \sim 64^{\circ}$. Morrison (1974) measured $T^* \sim 90 \pm 3^{\circ}\text{K}$ at 11μ and $T^* \sim 96 \pm 3^{\circ}\text{K}$ at 20μ when $\theta \sim 64^{\circ}$. Although these data indicate a change in the particle emissivity with the wavelength, we ignore it for simplicity and compare our theoretical brightness temperature with the data. Since the measurements of the brightness temperature were made at different distances from Saturn and the sun, we adjusted the above temperature data to the mean distance 9.5 A.U. from the sun. We computed the ring's isothermal black body temperature with three tilt angles

($\theta = 64^\circ, 72^\circ$ and 83°) for both cases (A) and (B). The results are shown in Figure 26. The upper and lower curves in Figure 26 are based on the cases (B) and (A), respectively. As is seen in Figure 26, the theoretical results based on the shadowing model used in this paper are compatible with the infrared brightness temperature data.

The preceding arguments are based on the assumption that the ring particles are uniformly heated and they emit thermal radiation from their entire surface. Let us consider the case of thermal emission from only one side of the ring particles. It is difficult to solve the radiative transfer problem in this case. We, therefore, consider only two heating sources, the solar heating and thermal emission from Saturn's ball. Thus, the effect of mutual heating among the ring particles is not included in the calculation of the isothermal black body temperature for the rings in this case. Even so, we find that the computed temperature in this case is about equal to the brightness temperature including the effect of three different heating sources in the case of uniformly heated ring particles. We, therefore, expect to have higher IR brightness temperature if the effect of mutual heating is included. This indicates that slightly higher optical albedos for the ring particles are allowed in the case of thermal emission from only one side of the ring particles. Such a case would apply approximately if the ring particles were synchronously rotating. We can estimate the size of the ring particles required to obtain synchronous rotation through the frictional dissipation of

of tides by Saturn within the age of the solar system (cf. Goldreich and Soter, 1966). Ferrin (1974) has made such a computation and obtained the lower limit of the size of the ring particles to be ~ 40 m, in order for them to rotate synchronously at the present day. This indicates that the ring particles whose size we have found in the preceding argument ($\langle \rho^2 \rangle^{1/2} \lesssim 4.5$ m) must emit thermal radiation from their entire surface and rotate rapidly.

In summary, we may match the IR data in the case that the rings are polydisperse with a size distribution such as equation (34) and $s = 2$, even if there exists considerable uncertainty in the albedo in the red. Although the monodisperse model works well with the optical data, it seems difficult to satisfy the high infrared temperature because of its higher optical albedo.

Figure 24: Theoretical IR brightness temperature distribution versus the optical depth in the ring layer.

T^{\odot} = temperature due to absorbed solar flux.

$T^{\odot+D}$ = temperature due to absorbed solar flux plus the mutual heating among the ring particles.

$T^{\odot+D+h}$ = temperature due to absorbed solar flux, mutual heating, and the flux from Saturn's ball.

These results are based on the case A for the ring particle albedo (see Figure 20).

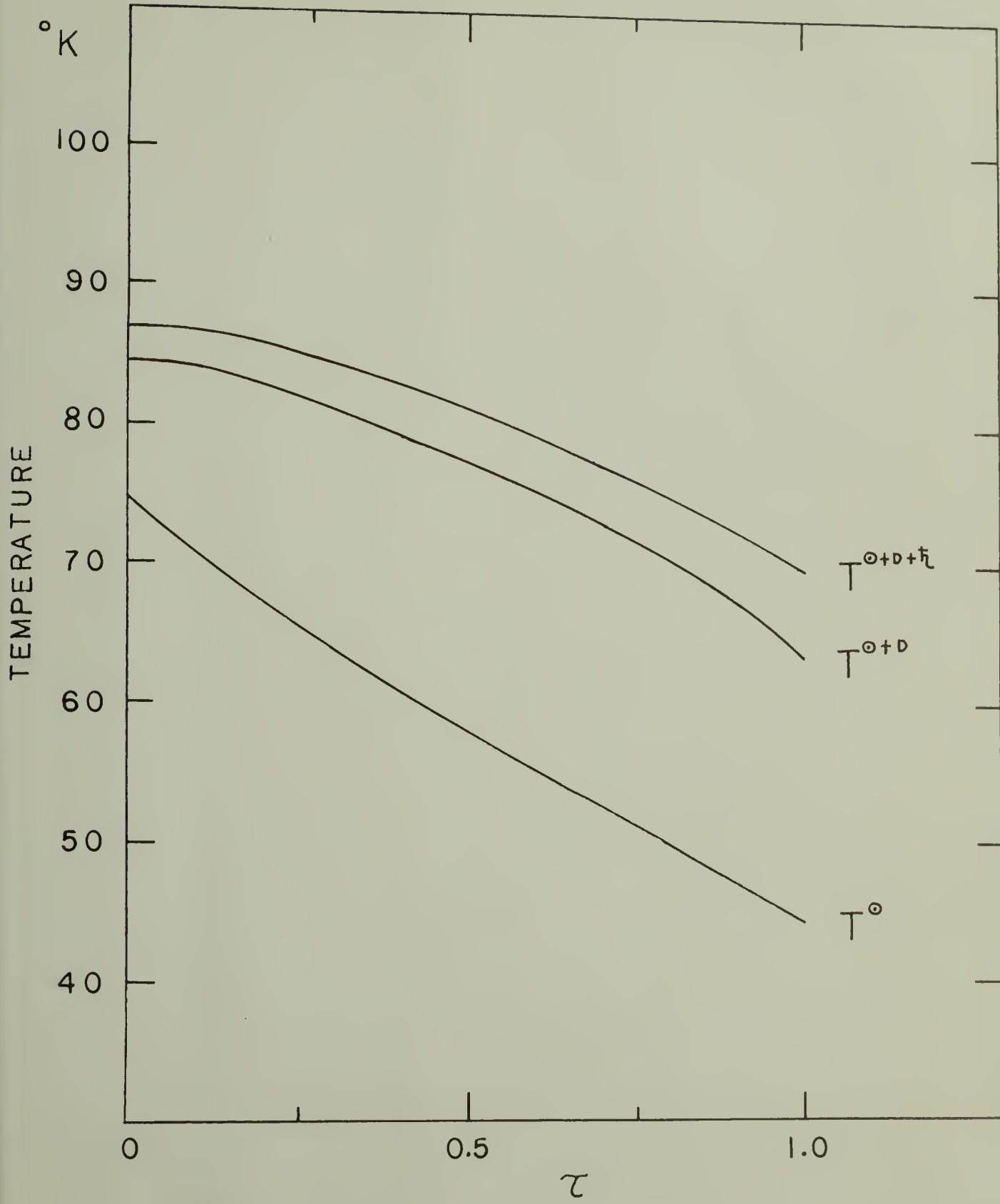


Figure 25: Theoretical IR brightness temperature distribution versus the optical depth in the ring layer. Same notation as Figure 24. These results are based on the case B for the ring particle albedo (see Figure 20).

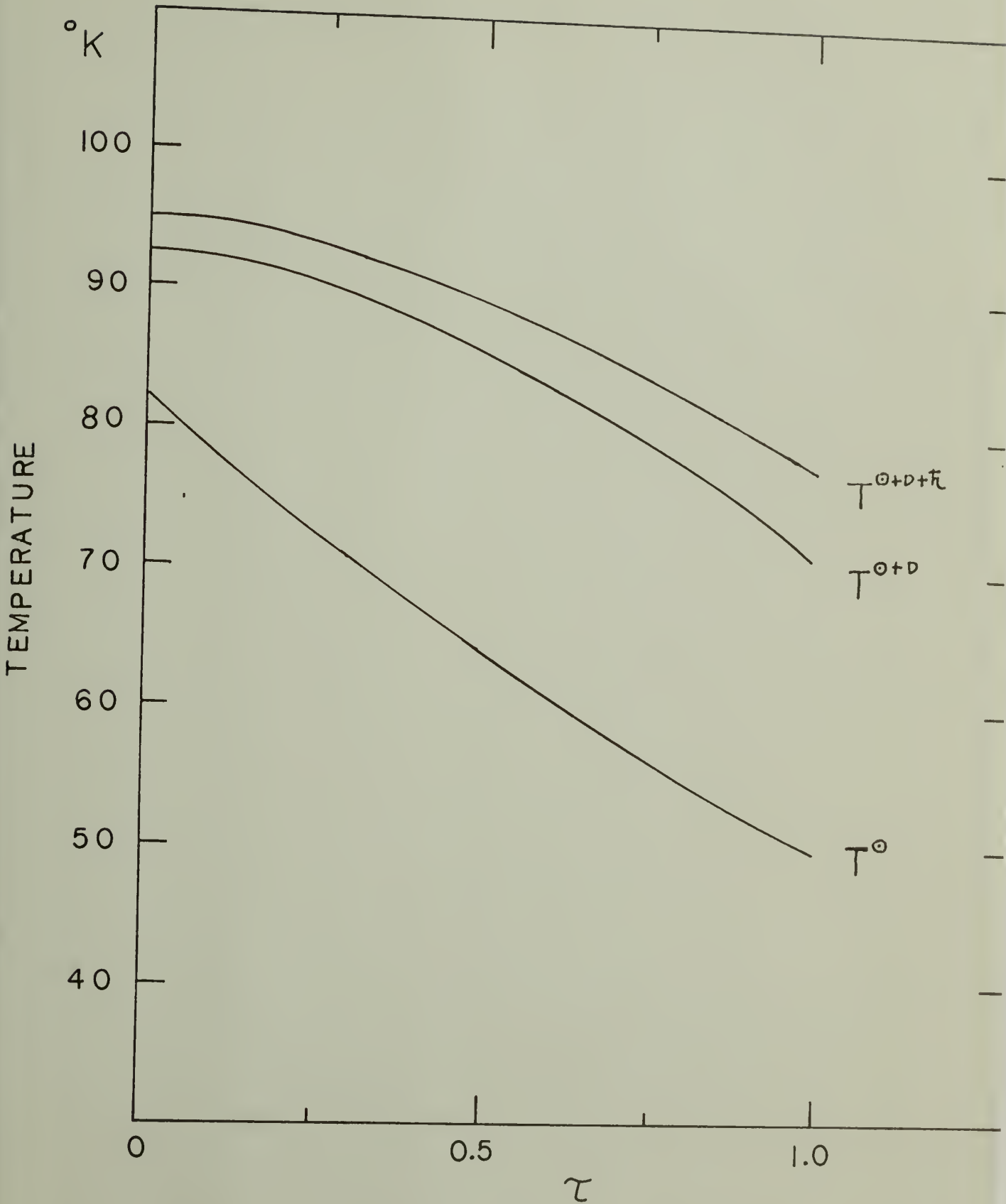
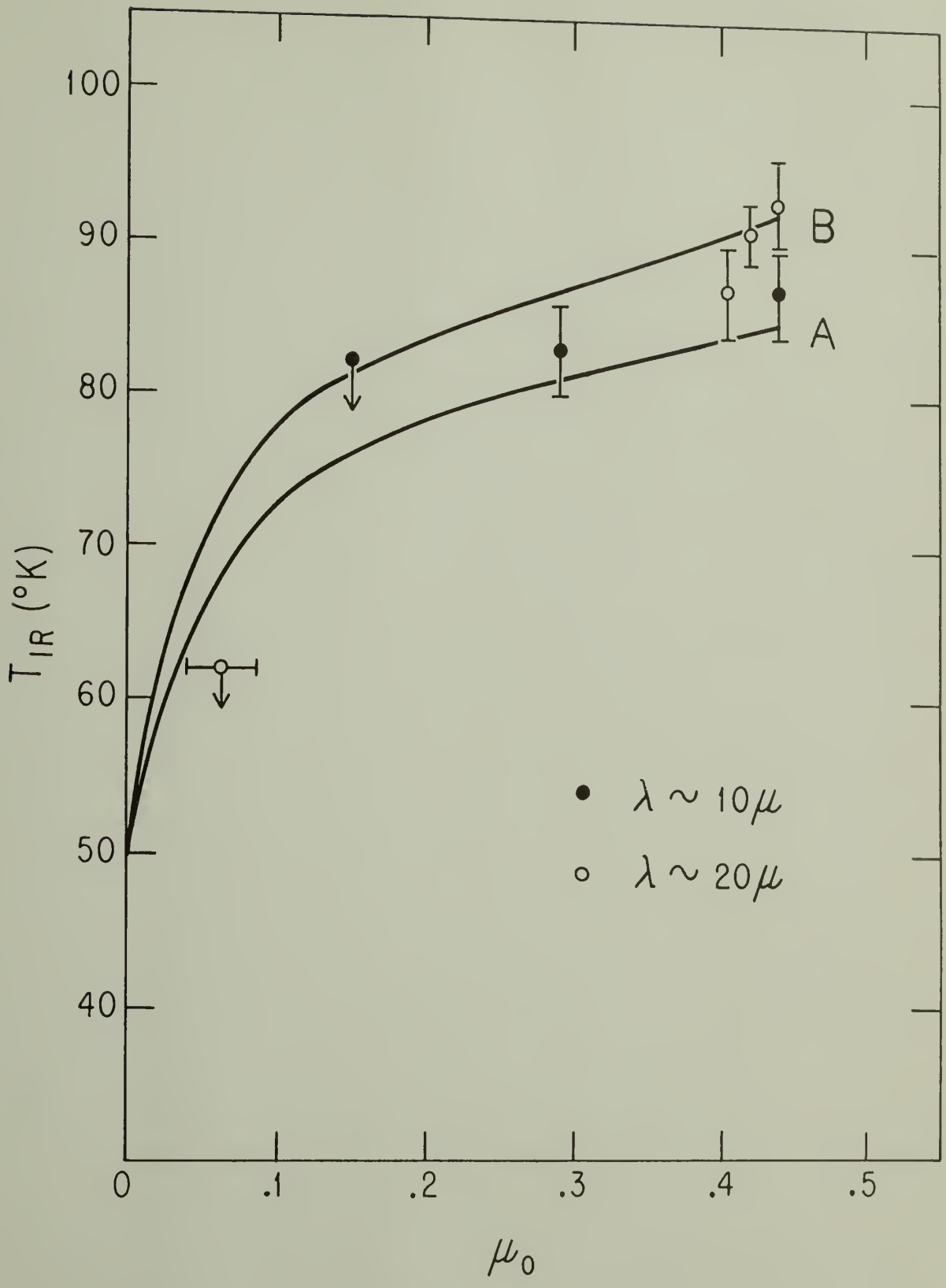


Figure 26: IR brightness temperature for ring B versus $\mu_0 = \cos \theta_0$.
Data taken from the compiled table of Murphy and adjusted to 9.5 AU. The curve A and B are based on the cases A and B for the ring particle albedo (see Figure 20).



SECTION VII

CONCLUSION

The basic models which were investigated in this thesis are based on the assumption that the rings form a layer many particles thick. More specifically, we assumed that a plane-parallel and homogeneous ring layer consists of many independent and randomly oriented spherical particles and that these particles are large enough and their number density is great enough to cast shadows upon each other. Under these assumptions we investigated models of Saturn's rings which include this shadowing mechanism, realistic phase functions for the individual ring particles, and the effects of multiple scattering and a particle size dispersion. In the shadowing mechanism we included the effects due to the finite size of the sun, including the penumbra. In the calculation of the IR brightness temperature of the rings, the effect of mutual heating among the ring particles was considered qualitatively for the first time.

The basic conclusions are the following. An appropriate model of the rings which matches the observed data in both optical and infrared regions of the spectrum seems to be the polydisperse case with the particle size distribution given by equation (34) and $s = 2$. The monodisperse case fails to satisfy the infrared data. Of course, we would expect on physical grounds that there would be a range of particle size in the rings. The actual form of the particle size distribution function can not be deduced from the measured data, but the presence of the additional parameter describing the size distri-

bution allows more flexibility in determining the albedo a so that lower values of a where are necessary to match the IR observations become possible. The size distribution cannot, however, be too flat (for then we have essentially the monodisperse case) or too steep (a predominance of very small particles does not produce sufficient shadowing effect). The lower limit of the optical thickness of ring B is larger than 0.5 in the visual wavelength band. The volume density D for ring B is close to 0.01. The ring particle phase function is somewhat backscattering which explains the linearly increasing part in the phase curve of the rings. Although the values of the phase integral depend on the choice of the parameter of the size distribution, their lower limits are $q_B \sim 1.0$ and $q_V \sim 1.4$ in B and V which agree with the results of Veverka (1973) for snow covered objects. The upper limit of the mean particle size $\langle \rho^2 \rangle^{1/2}$ is found to be less than 4.5 μ m for the polydisperse $s = 2$ model. The lower limit on particle size and the mean particle size remain uncertain. The particle Bond albedos in the blue and the visible are close to the lower limits of the particle albedo found in the polydisperse case $s = 2$. They are found to be $a_B \sim 0.42$ and $a_V \sim 0.72$, respectively.

The upper limit of the mean particle size found in this model agrees with both the models suggested by Pollack et al. (1973) and Pettengill and Hagfors (1974) to fit the microwave and radar data. The high albedo for the ring particles agrees with the deduction from the spectral data (Lebofsky et al.) that the principal constituent of at least the outer portions of the ring particles is ice, slightly

reddened by either the action of high energy radiation or the presence of impurities.

To clarify a lot of uncertainty in the red and near infrared regions, and thus to significantly refine the precision with which the ring parameters may be deduced from our model, we should stress again the desirability of reflectivity observations on an absolute scale beyond 1 micron and a good observational phase curve for the rings at wavelengths $\lambda \gtrsim 0.7\mu$.

REFERENCES

- Allen, C.W., 1963, Astrophysical Quantities, (University of London Press, London).
- Allen, D.A., and Murdock, T.L., 1971, *Icarus* 14, 1.
- Bobrov, M.S., 1940, *Astr. Zh.* 17, 1.
- Bobrov, M.S., 1956, *Astr. Zh.* 33, 161; 904.
- Bobrov, M.S., 1961, *Astr. Zh.* 38, 669.
- Bobrov, M.S., 1970, Surfaces and Interiors of Planets and Satellites (edited by Dollfus, A., Academic Press, London & N.Y.), p. 376.
- Camichel, H., 1958, *Annls. Astrophys. Paris* 21, 231.
- Cook, A.F., and Franklin, F.A., 1964, *Astr. J.* 69, 173.
- Cook, A.F., and Franklin, F.A., 1966, *Astr. J.* 71, 10.
- Cook, A.F., Franklin, F.A., and Palluconi, F.D., 1973, *Icarus* 18, 317.
- Cuzzi, J.N., and Van Blerkom, D.J., 1974, *Icarus* 22, 149.
- Deirmendjian, D., 1962, Mem., RM-3228-PR, the Rand Corp.
- Ferrin, I., 1974, D.P.S. Meeting, Palo Alto, California.
- Focas, J., and Dollfus, A., 1969, *Compt. Rend.* 268, 100.
- Franklin, F.A., and Cook, A.F., 1965, *Astr. J.* 70, 704.
- Goldstein, R.M., and Morris, G.A., 1973, *Icarus* 20, 260.
- Guthnick, P., and Prager, R., 1918, *Veröff. Sternw. Berlin-Balbesberg* 2.
- Hansen, J.E., 1969, *Ap. J.* 155, 565.
- Hertzsprung, E., 1919, *Astr. Nachr.* 208, 81.
- Irvine, W.M., 1964, *Bull. Astron. Insts. Netherlands* 17, 266.
- Irvine, W.M., 1965, *J. Opt. Soc. Amer.* 55, 16.

- Irvine, W.M., 1966, *J. Geophys. Res.* 71, 2931.
- Irvine, W.M., and Pollack, T.B., 1968, *Icarus* 8, 324.
- Irvine, W.M., and Lane, A.P., 1973, *Icarus* 18, 171.
- Jeffreys, H., 1947, *Mon. Not. R. Astr. Soc.* 107, 263.
- Kharitonova, G.A., and Teifel, V.G., 1973, *Astron. Tsirk.* No. 747.
- Kiladze, R.I., 1969, *Abastumani Astrophys. Obs. Bull.* No. 37, 151.
- Kuiper, G.P., 1949, *The Atmospheres of the Earth and Planets*
(University of Chicago Press, Chicago), p. 340.
- Kuiper, G.P., Gruikshank, D.P., and Fink, U., 1970, *Sky and Telescope*
39, 14.
- Lebofsky, L.A., Johnson, T.V., and McCord, T.B., 1970, *Icarus* 13, 226.
- Liou, K.-N., and Hansen, J.E., 1971, *J. Atmos. Sci.* 28, 995.
- Low, F.J., 1965, *Lowell Obs. Bull.* 5, 184.
- Low, F.J., 1966, *Astr. J.* 71, 291.
- Lumme, K., 1970, *Astrophys. Space Sci.* 8, 90.
- Maxwell, J.C., 1859, *Scientific Papers of J.C. Maxwell* (1890), 1,
(Cambridge University Press, Cambridge).
- Mihalas, D., 1967, *Methods in Comp. Physics* 7, (edited by Alder, B.,
Fernbach, S., and Rotenberg, M., Academic Press, London & N.Y.), p. 1.
- Mihalas, D., 1970, *Stellar Atmospheres* (Freeman and Company,
San Francisco).
- Morrison, D., 1974, *Saturn's Rings Workshop*, J.P.L.
- Murphy, R.E., Cruikshank, D.P., and Morrison, D., 1972, *Bull. AAS* 4.
- Murphy, R.E., 1973, *Ap. J.* 181, L87.
- Murphy, R.E., 1974, *Saturn's Rings Workshop*, J.P.L.

- Müller, G., 1893, Publ. Obs. Potsdam 8, 193.
- Pettengill, G.H., and Hagfors, T., 1974, Icarus 21, 188.
- Pierce, A.K., and Waddell, J.H., 1961, Mem. Roy. Astron. Soc. 68, 89.
- Pilcher, C.B., Chapman, C.R., Lebofsky, L.A., and Kieffer, H.H., 1970, Science 167, 1372.
- Pollack, T.B., Summers, A., and Baldwin, B., 1973, Icarus, 20, 263.
- Price, M.J., 1973, Astr. J. 78, 113.
- Rougier, G., 1934, L'Astronomie 48, 220; 281.
- Seeliger, H., 1887, Abhandl. Bayer. Akad. Wiss., Math.-Natur., Kl. II, 16, 405.
- Seeliger, H., 1895, Abhandl. Bayer. Akad. Wiss., Math.-Natur., Kl. II, 18, 1.
- Schoenberg, E., 1933, Vjschr. Astr. Ges. Lpz. 68, 387.
- Van de Hulst, H.C., 1948, Ap. J. 107, 220.
- Van de Hulst, H.C., 1957, Light Scattering by Small Particles (John Wiley & Sons, Inc., New York).
- Van de Hulst, H.C., and Irvine, W.M., 1963, La Physique des Planetes (11th Liege Ap. Symp.), 78.
- Veverka, J.G., 1973, Icarus 20, 304.

